Timing and extent of glaciation since the Last Glacial Maximum in the upper Kalguty basin, Russian Altai Mountains

Philip Deline, Ludovic Ravanel, Jean-jacques Delannoy, Melaine Le Roy, Team Aster, Laëtitia Leanni, Dimitri Cheremisin, Lydia Zotkina, Catherine Cretin, Jean-michel Geneste, et al.

JOURNAL OF QUATERNARY SCIENCE (2023) 1–21 ISSN 0267-8179. DOI: 10.1002/jqs.3535

JQS Journal of Quaternary Science QRA Quaternary Research Association

Timing and extent of glaciation since the Last Glacial Maximum in the upper Kalguty basin, Russian Altai Mountains

PHILIP DELINE,[1]* LUDOVIC RAVANEL,[1] JEAN-JACQUES DELANNOY,[1] MELAINE LE ROY,[1] ASTER TEAM,[2,†] LAËTITIA LÉANNI,[2] DIMITRI V. CHEREMISIN,[3] LYDIA V. ZOTKINA,[3] CATHERINE CRETIN,[4,5] JEAN-MICHEL GENESTE,[4] HUGUES PLISSON[4] and VYACHESLAV I. MOLODIN[3]

[1]Environnements, Dynamiques et Territoires de Montagne, Université Savoie Mont Blanc, Centre National de la Recherche Scientifique, Chambéry, France

[2]Centre Européen de Recherche et d'Enseignementdes Géosciences de l'Environnement, Aix-Marseille Université, CNRS, Institut de Recherche pour le Développement, Collège de France, Institut national de recherche pour l'agriculture, l'alimentation et l'environnement, Aix-en Provence, France

[3]Institute of Archeology and Ethnography of the Siberian Branch of the Russian Academy of Sciences, Novosibirsk, Russia

[4]Université de Bordeaux, CNRS, Ministère de la Culture, De la Préhistoire à l'Actuel: Culture, Environnement et Anthropologie, Pessac, France

[5]Musée National de Préhistoire, Les Eyzies, France

Received 16 November 2022; Revised 17 March 2023; Accepted 6 May 2023

ABSTRACT: The mountains systems of Central Asia are primary targets to study late Pleistocene climate evolution given their location at the crossroads of several atmospheric circulation systems. The timing of glacier extent during this period remains understudied, especially in the Altai Mountains. Here, we have reconstructed glacier extent during three main Late Pleistocene stadials in the upper Kalguty basin (south-eastern Russian Altai) based on field-based geomorphic analysis. Additionally, surface exposure dating with ^{10}Be and ^{26}Al at a key site was used to infer a minimum-limiting age for the outermost well-preserved Pleistocene frontal moraine system and to date the inception of glacier withdrawal. According to our data, around 20.6 ± 1.8 ka Kalguty Glacier was still 200 m thick at the key site, 10 km upstream of the outermost moraine, and the site was totally deglaciated shortly after 20.4 ± 0.4 ka. These results point to a rapid retreat of this low-gradient valley glacier after its probably MIS 2 maximum which was prior to 21 ka and probably prior to 22.5 ka. Two other glacier stages have been identified upvalley, characterized by a depression of the equilibrium-line altitude of 420 and 314 m with respect to the Little Ice Age, thus corresponding to Lateglacial advances. Our glacier reconstruction further provides a geomorphological and geochronological background to put into context archaeological findings in this area. © 2023 John Wiley & Sons, Ltd.

KEYWORDS: Altai; glaciation; Lateglacial; MIS 2; surface exposure dating

Introduction

Glacier extent is widely used for palaeoclimatic and environmental reconstruction as glaciers are reliable climatic indicators (Mackintosh et al., 2017). In the Russian Altai Mountains (Figure 1), numerous cataclysmic flood landforms (flood-scoured gorges, giant bars, gravel dunes) indicate the repeated occurrence of glacial megafloods during the late Pleistocene, *c.* 28–15 ka (Herget et al., 2020) as well as during Marine Isotope Stage (MIS) 5, *c.* 85 ka (Svistunov et al., 2022), with peak discharge of 10–18 × 10^6 m^3 s^{-1} (Baker et al., 1993; Herget, 2005), making glacier reconstruction especially relevant in this area. Several reconstructions of the extent of Late Pleistocene maximum advances in the Altai Mountains have been proposed (Figure 1; Lehmkuhl et al., 2011; Blomdin et al., 2016). However, knowledge of the timing of glacier advance during the last glacial cycle remains open in the Russian Altai Mountains (Agatova et al., 2012; Gribenski et al., 2016, 2017; Herget et al., 2017; Ganyushkin et al., 2018a; Herget et al., 2020), where the extent and timing of Lateglacial re-advances have been understudied.

Small glacier systems isolated from main ice masses are expected to provide best-preserved remnants to reconstruct past glacier extent (e.g. Pallàs et al., 2010). Here, we focus on a medium-sized glacier basin located close to the Tavan Bogd Massif at the south-eastern margin of Plateau Ukok, where one of the main glaciation centres of the Altai Mountains during the Pleistocene was located (Lehmkuhl et al., 2011). The present study was motivated by ongoing archaeological research developed by a joint Russian–French team since 2010 on the Ukok Plateau, and especially in the Kalguty basin (Cheremisin et al., 2015). The Altai Mountains are well known for their rich archaeological legacy with sites encompassing the Pleistocene (Denisovan Man; Slon et al., 2018) to the late Holocene (Scythian culture; Parzinger, 2017), as well as a new hotspot for glacial archaeology (Taylor et al., 2021). Numerous petroglyph sites exist in the region but are difficult to date given the absence of stratigraphy. Glacio-geomorphological investigations could help to provide a temporal framework, due to the dependence of human occupation on glacial dynamics during the Pleistocene. To address this issue, Deline et al. (2020) carried out a detailed geomorphological study of the upper Kalguty basin. Here we describe new surface exposure ages at one site to propose a relative chronology of glacial extents in the study area since the local Last Glacial Maximum (LGM) that might be not valid for other regions in the Altai Mountains due to the location of the upper Kalguty basin regarding moisture supply by westerly circulation.

*Correspondence: Philip Deline, as above.
Email: philip.deline@univ-smb.fr
†The ASTER Team comprises Georges Aumaître, Didier L. Bourlès†, Régis Braucher and Karim Keddadouche.

Figure 1. Location of the Ukok Plateau, Russian Altai Mountains (map location in the inset). Light white: glacier extent during the Late Pleistocene maximal advance (Blomdin et al., 2016); light blue: at present (RGI 6.0, RGI Consortium (2017). Black polygon: studied upper Kalguty basin; red line: national boundaries. Topography: 30-m ASTER GDEM. [Color figure can be viewed at wileyonlinelibrary.com]

Study area

The Russian Altai Mountains and the Ukok Plateau

The Ukok Plateau is a highland area with elevation ranging from 2000 to 3000 m asl, and that borders Kazakhstan, China and Mongolia. Access to the area is limited by steep, tall and glaciated mountain ranges: Katun range, the highest point in the Altai Mountains (Mount Belukha, 4506 m asl) to the west, South Chuya Range (3936 m) to the north, Tavan Bogd Massif (4374 m) to the south and Saylyugem Range (3502 m) to the east (Figure 1). The focus of this study is the Kalguty basin in the south-eastern part of the Ukok Plateau.

The Ukok Plateau is part of the Altai–Mongolian terrane in the north-western Central Asian Orogenic Belt (i.e. the Altai–Sayan Fold Belt; Glorie et al., 2011). This terrane is separated from the Gorny Altai terrane to the north by the Charysh–Terekta–Ulagan–Sayan suture–shear zone (Chen et al., 2014). It is dominated by thick Cambrian–Ordovician terrigenous sedimentary sequences resulting from flysch deposition, intruded by extensive Late Silurian–Devonian–Early Carboniferous granitoids and volcaniclastic sedimentary rocks (Glorie et al., 2011; Chen et al., 2014).

Mean monthly temperature at Akkem station (2056 m asl) was −18°C in January and +11°C in July for the period 1952–2004; mean summer (JJA) temperature increased by 0.1°C a^{-1} from 1985 to 2004 (Shahgedanova et al., 2010) and from 12 to 14.5°C over the period 1985–2015 at Kosh-Agach (1759 m asl, Figure 1; Ganyushkin et al., 2022). Too far north to be affected by the summer East Asian monsoon, the Russian Altai Mountains are today exposed to the westerlies (Benn & Owen, 1998). Annual precipitation ranges from >800 mm in the north and 500–700 mm in the north-west to <200 mm along the border with Mongolia (Shahgedanova et al., 2010; Batbaatar et al., 2017): 111 mm a^{-1} at Kosh-Agach for instance (Ganyushkin et al., 2017). The strong winter Siberian high centred on the Altai is the reason that 35–65% of the annual precipitation occurs in summer (Khandsuren et al., 2019); mean winter precipitation is 27 mm a^{-1} at Kosh-Agach (Batbaatar et al., 2017; Gribenski et al., 2017). Finally, estimated vertical temperature and precipitation gradients are 0.56°C 100 m^{-1} and 20 mm 100 m^{-1} in the west area of the Tavan Bogd north side, 25 km south-west of our study area (Ganyushkin et al., 2017). However, the circulation pattern was probably modified in Pleistocene times (Herget et al., 2020), leading to changes of the glaciation dynamics in the Russian and Mongolian Altai Mountains. Therefore, as our study area is located in the area in between, taking current climate data into account is challenging.

A large part of the Altai Mountains was glaciated during the Late Pleistocene maximal advance (Fig. B). Altai Mountains

glaciers covered 2288 km^2 during the Little Ice Age (Ganyushkin et al., 2022), and 1096 ± 53 km^2 in 2020 (Chang et al., 2022; Ganyushkin et al., 2022), representing presently *c.* 50% of the glacierized area of North Asia (RGI Region 10; Earl & Gardner, 2016). In the Russian Altai Mountains, glaciers are mainly located at present in the Katun (185 km^2), North (129 km^2) and South Chuya (135 km^2) Ranges, mainly on their north side, and on the Tavan Bogd north side (23.5 km^2), totalling 483.5 km^2 (RGI Consortium, 2017; Figure 1). They have retreated during the 20th century, with a loss of 20% from 1952 to 2004 in response to an increase of 1.26°C in summer temperature at 2050 m asl and in spite of a slight increase (14%) in precipitation at the highest elevations (Shahgedanova et al., 2010; Earl & Gardner, 2016). A loss of 12 ± 3% occurred from 2000 to 2020, with a shrinkage rate of −0.60% a^{-1} (Chang et al., 2022). Shrinkage rate in the South Chuya Range increased from −0.17% a^{-1} in 1952–2008 to −0.45% a^{-1} in 2000–2020 (Chang et al., 2022). Mean ELA (equilibrium-line altitude) was 3184 m over the 1962–2012 period at Maliy Aktru Glacier (North Chuya Range; WGMS, 2021), and *c.* 3500 m over the 1980–2018 period at Potanin Glacier (Tavan Bogd east side, Mongolia; Khalzan et al., 2022). Modelled recent ELA for the Altai Mountains shows a NW–SE gradient, from 2600 m in the north-west to 2900–3000 m in the Katun Range (Lehmkuhl et al., 2004; Lehmkuhl, 2008), 3300–3350 m in the South Chuya Range (Lehmkuhl et al., 2011), and 3358 m in the Tavan Bogd Massif (Ganyushkin et al., 2022).

The Altai Mountains are affected by permafrost (Gruber, 2012). Spatial modelling suggests that continuous permafrost characterizes the slopes of the study area, and sporadic permafrost characterizes the floor of the main valley (Marchenko et al., 2006; Riseborough et al., 2008). In the Mongolian Altai Mountains, estimated permafrost thickness is in the range 60–250 m between 2200 and 2950 m asl, and the active layer 1–5 m (Walther et al., 2017; GTN-P Database, 2019). In the Chuya River catchment, the lowest indicators of permafrost are found at 1300 m asl near Aktash, and active pingos at 2000 m near Beltir, 35 km west of Kosh-Agach (Herget, pers. comm. 2023).

The upper Kalguty basin

The upper Kalguty basin is located along the border with Mongolia (Figure 2). The gentle hills to the north reach slightly above 3000 m asl; the crest-line of the steep Saylyugem Range on the opposite side is broadly above 3000 m, culminating at the Tundu-Uqgar (3529 m). The valley floor falls from 3000 to 2300 m over a distance of 22 km. Modelled annual precipitation is in the range 100 mm, with 65% in summer (JJA; Batbaatar et al., 2017) to 200–300 mm (Klinge & Sauer, 2019). This very dry area is covered by an alpine meadow, replaced by a tundra-type vegetation above *c.* 3000 m.

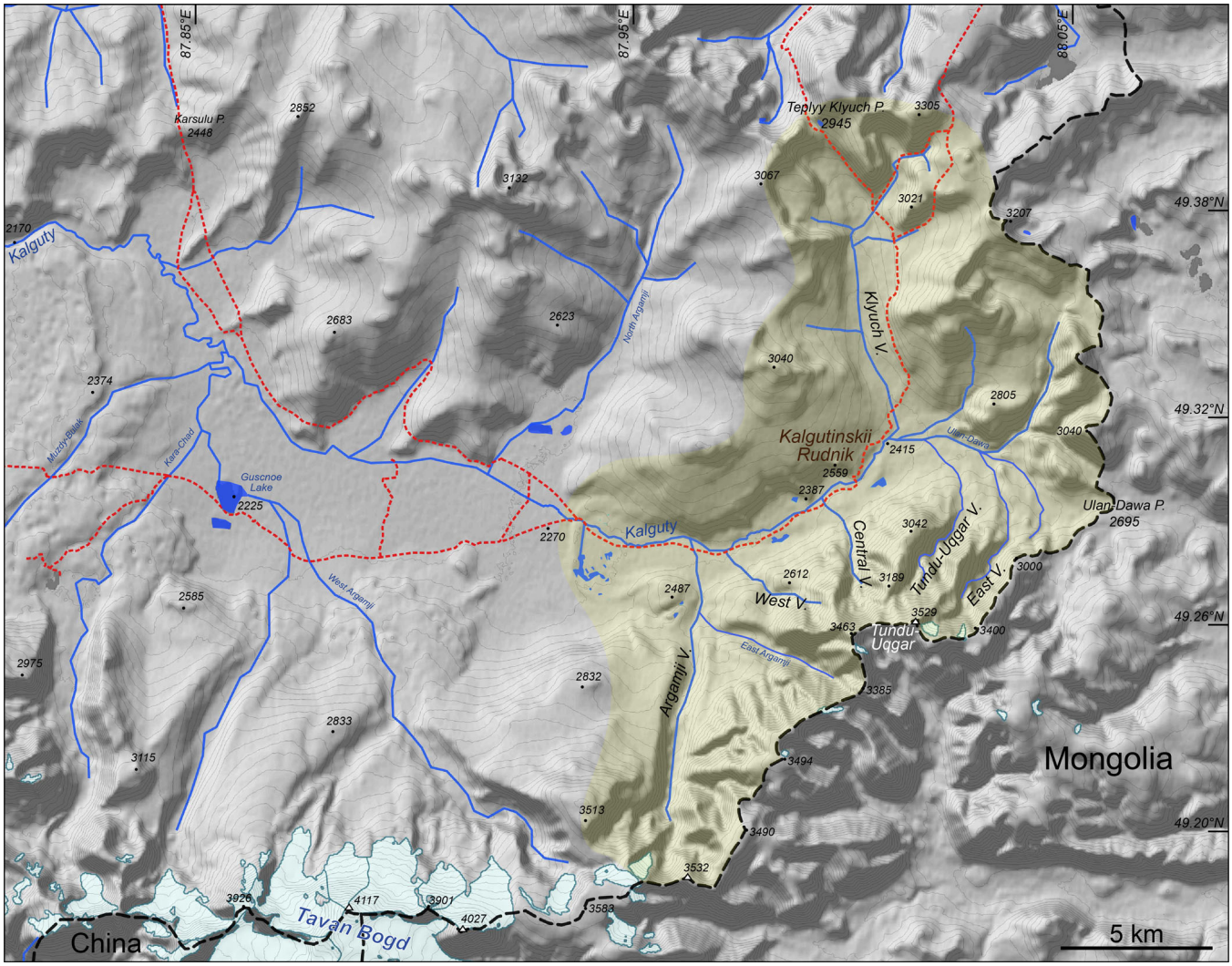

Figure 2. Upper Kalguty basin, south-east of the Ukok Plateau. V: valley; P.: pass; light yellow area: study area; light blue areas: present-day glacier extent according to RGI 6.0 (RGI Consortium, 2017); red-dotted line: four-wheel-drive trails; black-dashed line: national boundaries. Kalgutinskii Rudnik: main petroglyph site of the region. Topography: ESRI World Shaded Relief (contour line interval: 50 m). [Color figure can be viewed at wileyonlinelibrary.com]

Geological setting of the study area

The upper Kalguty basin is mainly incised in volcaniclastic sedimentary rocks. The Saylyugem side between the Ulan-Dawa and the East Argamji Rivers (Figure 2) is composed of conglomerates, sandstones, schists and quartzites, interbedded with marlstones and volcanic rocks (Early Devonian Ulandryk Formation). Felsic rocks (e.g. rhyolite) interbedded with sandstones and schists outcrop in the rest of the study area (Middle Devonian Aksay Formation). Both formations are cross-cut by a N120°E striking fault. The two small valleys to the north of the Ulan-Dawa river are aligned on secondary NE-striking faults (N10–40°E). Finally, a porphyraceous granite batholith with aplite dykes crops out at the head of the Klyuch Valley and forms the massif through which the Teplyy Klyuch pass (2945 m asl), allowing access to the Kalguty basin from the north (Figure 2).

Geomorphology of the study area

In this section we summarize the relevant non-glacial landforms and deposits described by Deline et al. (2020). Landforms and deposits related to the glacier dynamics in the upper Kalguty basin are fully described in the Results. Full deglaciation of the basin allowed the expression of periglacial, landslide and torrential processes, the periglacial processes mainly giving the present aspect to the landscape (Figure 3). Rock fall is active as shown by the numerous fresh scree deposits. The slopes of the south side are mainly covered by

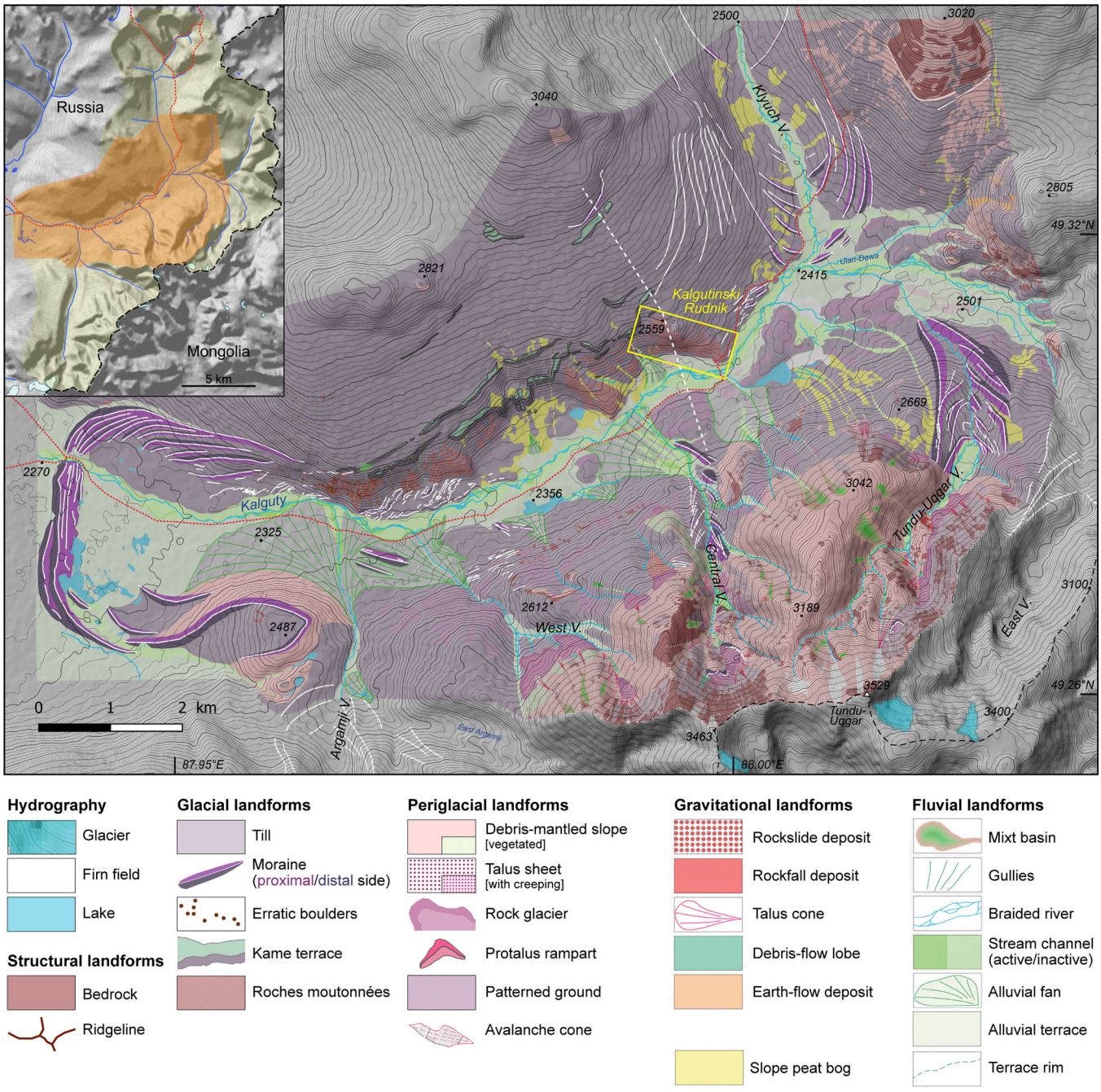

Figure 3. Geomorphological map of the central part of the upper Kalguty basin (Deline et al., 2020). V: valley; white lines: moraine crests; glaciers: present-day extent according to RGI 6.0 (RGI Consortium, 2017); yellow rectangle: dating site of Kalgutinskii Rudnik; white-dashed line: cross-section on Figure 8C; red-dotted line: four-wheel-drive trails; black-dashed line: boundary between Russia and Mongolia (shaded 30-m DEM from ASTER; contour line interval: 10 m). Inset map: light yellow area: study area; orange area: spatial extent of the geomorphological map. [Color figure can be viewed at wileyonlinelibrary.com]

regolith resulting from frost wedging and heaving, with blockfields and block slopes, talus sheets and cones smoothed by snow avalanches. Rock glaciers, generally inactive or relict, are located at the foot of the slopes, and patterned ground is present on flat areas. Block streams and solifluction lobes characterize the north side of the basin.

The most remarkable landslide is the slow deformation of a long kame terrace on the north side of the Kalguty valley, incised by subparallel rills and small gullies (Figure 3). The south side is deeply carved by dendritic valleys, whose wide alluvial fans indicate high peak discharge. Finally, the braided channel of the Kalguty River is flanked by inactive, wetland-type channels, and low alluvial terraces (Figure 3).

Glaciers of the study area since the Little Ice Age

According to Ganyushkin et al. (2018b), 23 glaciers were present in the upper Kalguty basin during the Little Ice Age (LIA, i.e. 1820 CE), with a total area of 5.41 km^2 (Supporting Information Fig. S1; Table S1). The largest glacier (1.16 km^2) was located at the head of the East valley, while the 16 other glaciers in the Argamji valley were in the range 0.02–1.0 km^2 (total = 2.83 km^2). ELA depression in the basin during the LIA was 80 m compared to the beginning of the 21th century (Ganyushkin et al., 2015).

A glacier inventory in the region for 1980 by Redkin (1998) surveyed 11 glaciers in the upper Kalguty basin, with a total area of 4.28 km^2 (Fig. S1). Only three glaciers are still present in the upper Kalguty basin according to the RGI 6.0 (RGI Consortium, 2017), located at the head of the East valley ($n = 2$; 0.25 km^2) and the Argamji valley (0.38 km^2; Fig. S1). This inventory is based on a SPOT 5 image from August 2011, but Pléiades images from September 2016 suggest that they were still present at least in the East valley. In 2010, the front elevation of the three glaciers was in the range 3150–3230 m, and their ELA in the range 3395–3425 m (Ganyushkin et al., 2018b). Seven additional small glaciers were recognized in the basin by Ganyushkin et al. (2018b), giving a total glacier area of 1.04 km^2 in 2010 (Fig. S1; Table S1). They are now mostly firn fields as observed in the Tundu-Uqgar valley in 2015 (Figure 3) – with some ice patches as suggested in mid-August 2019 by 10- to 20-m-resolution data from Sentinel-2 (using a red/SWIR band ratio: Paul et al., 2020).

Glacier shrinkage on the Tavan Bogd north side, characterized by larger glaciers, was 0.5, 0.9 and 0.1% a^{-1} during the periods 1962–2001, 2001–2009 and 2009–2015, respectively (Ganyushkin et al., 2017). Modelled ELA is 3300–3400 m in the region (Lehmkuhl et al., 2004; 2011; Ganyushkin et al., 2015); observed ELA elevation in 2015 was 3335 m on the Tavan Bodg north side and 3395 m on the Saylyugem Range (Ganyushkin et al., 2017) – an ELA of 3218 m was observed in 2021 (Ganyushkin et al., 2022). Although the shrinkage rate has decreased in the last of the three periods, current ELA elevation close to the crests and summits in the Kalguty basin explains the vanishing of its smaller glaciers.

Methods

Glacier geometry and ELA reconstruction

Based on high-resolution geomorphological mapping (Figure 3; Deline et al., 2020), we determined the palaeo-ice extent of the glaciers in the upper Kalguty basin from selected glacial markers: frontal and lateral moraines, and ridges delimiting the former accumulation zone. To reconstruct the palaeo-glacier surface topography, we used the GIS-based *GlaRe* toolbox (Pellitero et al., 2016). In addition to the glacier outlines, constrained by glacial markers, this program uses as inputs the manually drawn palaeo-glacier flowlines and the glacier bed topography, corresponding to the present digital elevation model (DEM). We did not remove postglacial sediment valley infill, as no data are available on its thickness and age, whereas studies suggest that pre-LGM sediment may not have been completely or eroded at all in glaciated valleys (James et al., 2019). To compute ice thickness, *GlaRe* iteratively solves an equation which assumes no basal sliding and glacier ice with a perfect plasticity rheology (Shilling & Hollin, 1981; Pellitero et al., 2016). The program allows for different basal shear stress values to be manually tuned along the flowlines, depending on the nature of the substratum. Basal shear stress is a critical input as it has a significant influence on obtained thickness data, especially in the case of our low-gradient glacier. Selected basal shear stress values were chosen to match geomorphological evidence and range here from 40 kPa in the flat and soft-sediment areas to 85 kPa on the rough terrains and 100 kPa in the cirques. These are lower values than the standard reference value of 100 kPa for alpine glaciers with rough subglacial topography (Paterson, 1994; Pellitero et al., 2016). This is because low shear stress values characterize low-angle glacier sectors with soft bed, such as the tongue of the reconstructed Kalguty paleoglacier. However, our selected values are fully in accordance with other works in similar settings (Gribenski et al., 2016; Blomdin et al., 2018; Radue, 2018).

Once the palaeo-surface is obtained, ELAs have been calculated using the toolbox of Pellitero et al. (2015). First, we considered the widely reported accumulation area ratio (AAR = 0.6 in this case). We also computed the accumulation ablation balance ratio (AABR) with a ratio of 1.75 according to Rea (2009).

^{10}Be surface exposure dating

Sampling for surface exposure dating

Sampling for surface exposure dating (SED) was focused on the site of the studied petroglyphs, Kalgutinskii Rudnik, an area of roches moutonnées ranging from 2410 to 2575 m asl. Three zones were defined based on topography, petroglyph style and density, and pattern of glacial striae (Figure 4). In each zone, four samples were extracted in July 2015 with hammer and chisel from scoured bedrock (rhyolite), veins of quartz, and top of granitic erratic boulders of metre size lying at its surface without signs of being moved or covered by sediments (Figure 4; Table 1). Large pieces of rhyolite were sampled to ensure obtaining a sufficient amount of quartz. The location and elevation of the samples were recorded with a handheld GPS, assuming a vertical and horizontal positional uncertainty of ±10 and ±5 m, respectively (Table 1). The shielding factor (Dunne et al., 1999), which results from dip/orientation of bedrock surface and topographic skyline shielding, was determined in the field with a clinometer and a compass. All samples were prepared for ^{10}Be and ^{26}Al analyses ($n = 12$). Analysis of paired nuclides allows insight into potential complex burial–exposure history of the corresponding boulders and bedrock surfaces (Nishiizumi et al., 1993; Fabel et al., 2002; Gjermundsen et al., 2015; Knudsen & Egholm, 2018).

^{10}Be and ^{26}Al geochemistry and AMS measurement

All ^{10}Be and ^{26}Al measurements were performed at CEREGE (Aix-en-Provence, France). Extraction of ^{10}Be

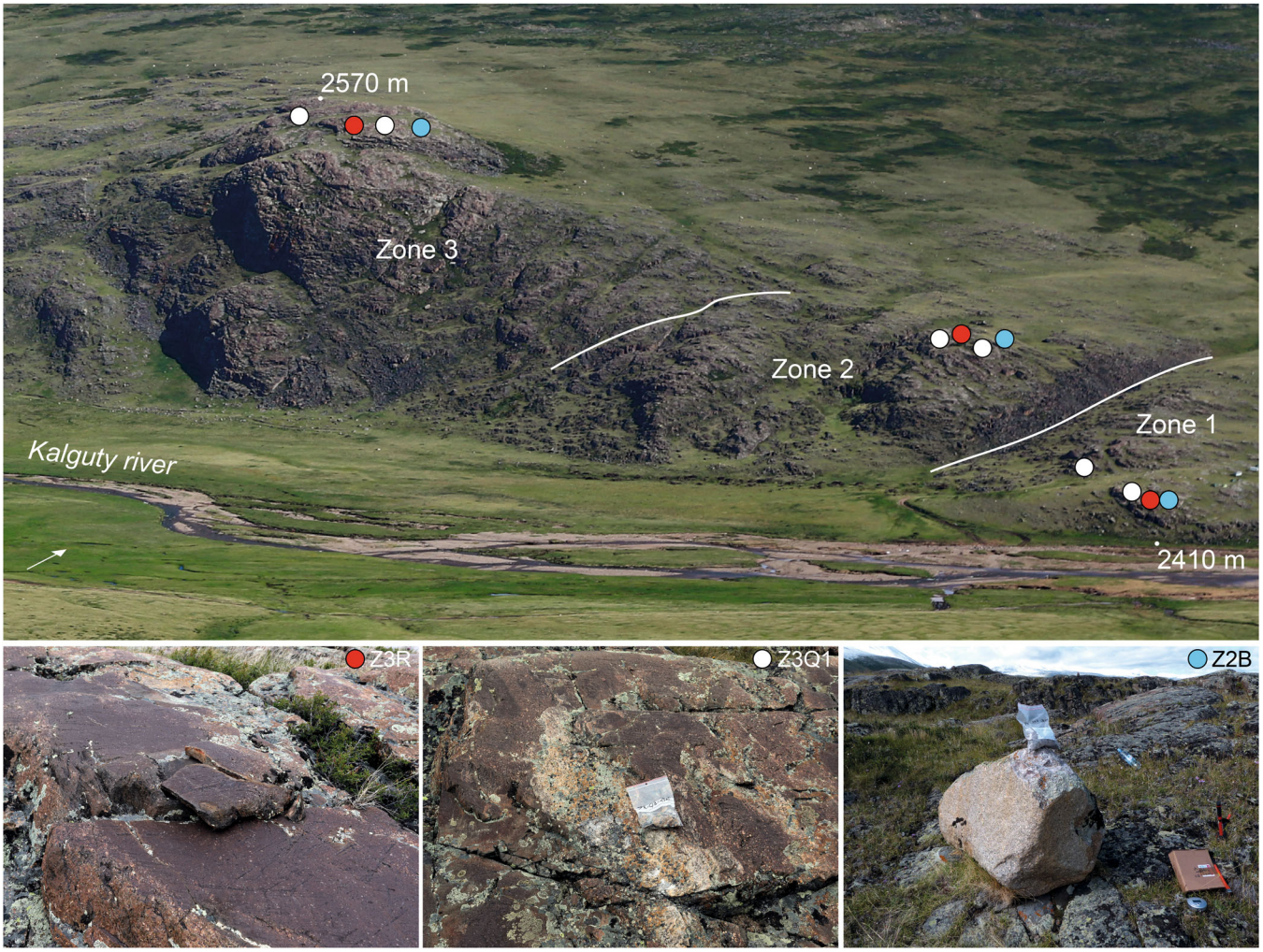

Figure 4. Location of the 12 samples extracted for SED in July 2015 on the engraved Kalgutinskii Rudnik. Samples from rhyolite bedrock: red dots; quartz vein: white dots; granitic boulder: cyan dots. Zones: see text; white arrow indicates north; elevations are in m asl. Insets: Three samples extracted from (left to right): rhyolite bedrock (Z3R); quartz vein (Z3Q1); granite boulder (Z2B). [Color figure can be viewed at wileyonlinelibrary.com]

Table 1. Sample characteristics from the petroglyph site Kalgutinskii Rudnik.

Sample	Lithology	Granitic boulder size, L × W × H (m)	Latitude, °N	Longitude,°E	Elevation (m asl)	Direction of dip/dip angle of sampled surface	Sample thickness (cm)	Shielding factor
Z1Q1	Quartz	—	49.304722	88.055833	2426	160°/16.0°	2.0	0.99505
Z1Q2	Quartz	—	49.304722	88.055833	2423	170°/23.8°	2.0	0.98602
Z1B	Granite	0.70 × 0.60 × 0.50	49.304722	88.055833	2424	-	2.0	0.99765
Z1R	Rhyolite	—	49.304722	88.055833	2424	160°/21.6°	5.0	0.99003
Z2Q1	Quartz	—	49.305000	88.052500	2469	190°/10.6°	2.0	0.99762
Z2Q2	Quartz	—	49.305000	88.052500	2465	190°/11.8°	2.0	0.98454
Z2B	Granite	0.94 × 0.53 × 0.84	49.305000	88.052500	2467	—	2.0	0.99810
Z2R	Rhyolite	—	49.305000	88.052500	2469	190°/10.6°	5.0	0.99762
Z3Q1	Quartz	—	49.306667	88.045833	2565	150°/16.0°	2.0	0.99644
Z3Q2	Quartz	—	49.306667	88.045833	2569	180°/27.0°	2.0	0.98247
Z3B	Granite	1.90 × 2.00 × 1.50	49.306667	88.045833	2557	—	3.0	0.99868
Z3R	Rhyolite	—	49.306667	88.045833	2566	180°/21.0°	5.0	0.99154

and ^{26}Al from the rock samples followed the chemical procedure of Brown et al. (1991) and Merchel & Herpers (1999). Samples were crushed and sieved and the 250- to 1000-µm fraction was processed. Quartz was concentrated through magnetic separation and selective dissolution in a 1/3 HCl – 2/3 H_2SiF_6 mixture. Quartz was decontaminated from the atmospheric ^{10}Be by dissolving 30% in mass through three successive HF leachings. Pure quartz was then spiked with 100 µL of a (3025 ± 9)-ppm in-house ^{9}Be carrier (Merchel et al., 2008), and with adapted amount of a 978 µg g^{-1} ^{27}Al commercial carrier (SCP Sciences). Natural ^{27}Al concentrations in the dissolved samples were measured by inductively coupled plasma optical emission spectrometry (ICP-OES) on an ICAP6500 Thermo Scientific unit spectrometer. Finally, dissolution was completed in concentrated HF.

BeO and Al_2O_3 were purified and extracted using a succession of alkaline precipitations and separations on ionic-exchange resins (exchange resins used: DOWEX 1 × 8 100–200 mesh, DOWEX 50 W × 8 100–200 mesh). Full oxidization was performed at 700°C. The obtained BeO and Al_2O_3 oxides were mixed with Nb and Ag conductive powders respectively, and then added to a copper cathode to be pressed. The $^{10}Be/^{9}Be$ and $^{26}Al/^{27}Al$ ratios were finally measured at the French national accelerator mass spectrometry (AMS) facility ASTER (Table 2). The measured $^{10}Be/^{9}Be$ ratios were calibrated against the $^{10}Be/^{9}Be$ STD-11 standard with an assigned value of $(1.91 \pm 0.013) \times 10^{-11}$ (Braucher et al., 2015). The measured $^{26}Al/^{27}Al$ ratios were calibrated against the ASTER in-house standard SM-Al-11 whose nominal value is $^{26}Al/^{27}Al = (7.401 \pm 0.064) \times 10^{-12}$ (Merchel & Bremser, 2004). The used half-lives [^{10}Be: 1.387 ± 0.012 Myr (Korschinek et al., 2010; Chmeleff et al., 2010); ^{26}Al: 0.717 ± 0.017 Myr (Samworth et al., 1972)] and the standardization method used at ASTER imply that the $^{26}Al/^{10}Be$ spallation production ratio is ~6.61 ± 0.52. AMS analytical uncertainties include the counting statistics, the machine stability [~0.5%; Arnold et al. (2010) for ^{10}Be] and the blank correction. The 1σ analytical errors averaged 4 ± 0.7% for ^{10}Be and 4.1 ± 0.9% for ^{26}Al. One sample (Z1B) was rejected at tests during ^{10}Be measurement.

The error-weighted average $^{10}Be/^{9}Be$ full-process blank ratio is $(2.94 \pm 0.44) \times 10^{-15}$. Blank correction accounts for 0.4–1.4%. $^{26}Al/^{10}Be$ ratios were calculated with the CRONUS-Earth exposure age calculator and referenced to 07KNSTD (Balco et al., 2008 and update from v. 2.2 to v. 2.3 published by Balco in June 2016; http://hess.ess.washington.edu/math/al_be_v23/al_be_multiple_v23.html). A rock density of 2.65 and 2.5 g cm^{-3} was used for granite and quartz samples and for rhyolite samples, respectively.

SED age computation

All ^{10}Be and ^{26}Al ages were calculated using the *iceTEA* online tool (http://ice-tea.org; Jones et al., 2019). It uses a modified version of the CRONUScalc calculation framework (Marrero et al., 2016) and global production rate calibration datasets (Borchers et al., 2016). Ages are reported using the time- and nuclide-dependent scaling scheme LSDn (or 'Sa'; Lifton et al., 2014). As a sensitivity test, age calculation was also made with the 'Lm' scaling scheme (Lal, 1991; Stone, 2000). These two scaling schemes provide lower and upper bounds, respectively, of ages which can be reasonably expected with state-of-the-art nuclide systematics. No snow correction was applied because of present low precipitation, especially during the cold season, while active wind blows the exposed surfaces. No erosion correction was applied, as glacial striations and a coating layer of glacial polish (Siman-Tov et al., 2017) are still present at the surface of the *roches moutonnées*, and the surface of granitic erratic boulders is generally slightly weathered (Figure 4). Mean surface ages were computed as the arithmetic mean and the standard deviation of the corresponding original ^{10}Be age data set.

Results and interpretation

Glacial landforms and deposits in the upper Kalguty basin

The most prominent glacial feature is a large set of terminal moraines that cross the valley bottom over a length of 3.5 km at the western end of the study area (Figure 5a). This terminal moraine extends up to 25 m high on its distal side and 15–20 m high on its proximal one; its is up to 500 m wide and includes several ridges of various sizes. With its base at 2275 m asl, the outermost moraine is slightly lower and less continuous than the first recessional moraine. This wide west morainic complex is continuous upstream by lateral moraines (Figure 5b). On the south side of the valley, the main moraine lies on a 100-m-high rock bump, above some recessional ridges; nested moraines have been deposited by accretion on the north side. The Kalguty Glacier lobe that built this impressive latero-frontal moraine loop had a surface area of *c.* 10 km^2.

Two *c.* 5-km-long narrow terraces continue upstream from the nested right-lateral moraines. Composed of sands and gravels, these are interpreted as kame terraces, standing 150 and 180 m above the valley floor at the west end, and 200 and 220 m at their eastern end (Figures 3 and 5b). Lobate-shaped deformations of the lower one resulted from creep processes favoured by rill runoff.

Upstream from the confluence of the Argamji and Kalguty Rivers, numerous small ridges are present at the base of the north side of the valley, up to 40 m above the river bed (Figure 5b). These recessional moraines can be connected to several larger ones at the bottom of the opposite side that are partly buried by alluvial fans (Figures 3 and 5b). Higher on this south side, a set of small subparallel ridges stands between 70 and 150 m above the valley floor. At the same elevation on the north side, below the lower kame terrace, bedrock is outcropping: a dense network of striations and the asymmetry of this scoured bedrock indicate *roches moutonnées*. Hundreds of metre-size erratic boulders are deposited on them, the

Table 2. Cosmogenic ^{10}Be and ^{26}Al data from the petroglyph site Kalgutinskii Rudnik.

Sample	Quartz dissolved (g)	^{9}Be spike (mg)	$^{10}Be/^{9}Be$	[^{10}Be] (at.g^{-1})	Error (at.g^{-1})	[^{26}Al] (at.g^{-1})	Error (at.g^{-1})	[Al-27] (μg g-)	$^{26}Al/^{10}Be$
Z1Q1	22.2613	100.26	6.5481E-13	593 449	23 501	3430 422	110 005	39.02	5.78 ± 0.29
Z1Q2	22.0540	100.44	6.1842E-13	566 595	17 998	3653 972	136 648	31.58	6.45 ± 0.32
Z1B	18.5956	100.45	—	—	—	2333 220	99 186	140.50	—
Z1R	8.9221	100.42	2.5264E-13	568 073	27 087	3156 123	170 810	249.18	5.56 ± 0.40
Z2Q1	21.1195	100.36	6.2988E-13	602 202	19 001	3619 500	115 625	30.66	6.01 ± 0.27
Z2Q2	20.5438	100.38	6.0768E-13	597 280	23 778	3742173	132 302	39.71	6.27 ± 0.33
Z2B	22.1734	100.44	7.2502E-13	661 158	25 793	3651 177	137 193	216.62	5.52 ± 0.30
Z2R	20.4603	100.35	6.5979E-13	651 198	28 753	2866 014	148 458	196.29	4.40 ± 0.30
Z3Q1	20.6299	100.42	6.6173E-13	648 202	21 231	3907 802	165 566	45.90	6.03 ± 0.32
Z3Q2	21.3791	100.41	7.5168E-13	710 825	37 759	3790 119	132 705	71.84	5.33 ± 0.34
Z3B	21.6466	100.39	7.9583E-13	743 285	25 401	2945 207	99 800	120.60	3.96 ± 0.19
Z3R	7.3945	100.40	2.1517E-13	582 451	28 722	4036 434	243 718	262.01	6.93 ± 0.54

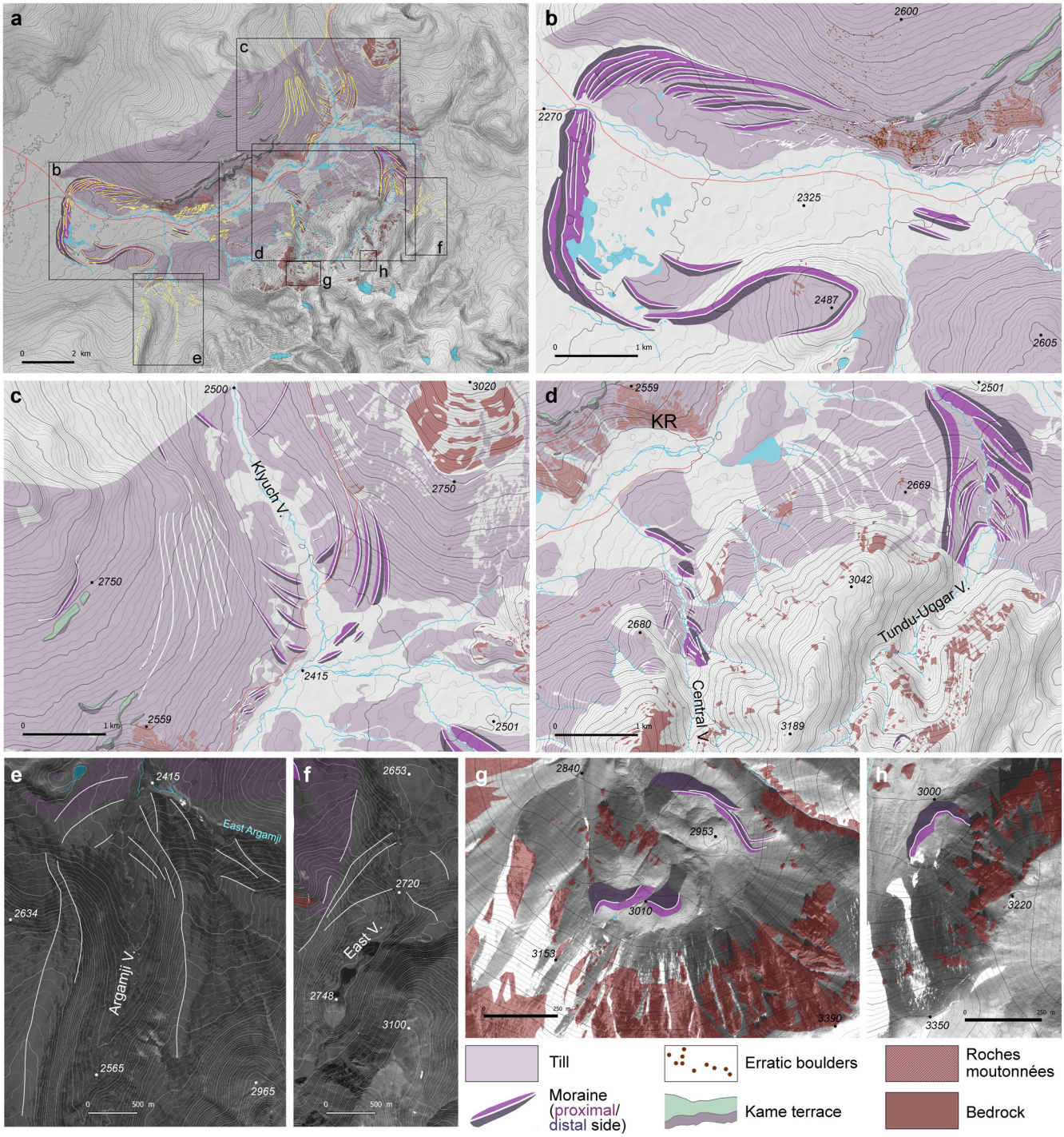

Figure 5. Markers of palaeo-extents of the glaciers in the upper Kalguty basin. (a) location of maps (b–h; b)b–h; (b) West morainic complex; (c) Klyuch morainic complex; (d) Central and Tundu-Uqgar morainic complexes; KR: Kalgutinskii Rudnik; (e) Argamji morainic complex; (f) East valley morainic complex; (g and h) head of Central and Tundu-Uqgar valleys, respectively. White lines (yellow in a): moraine crests. Contour line interval: 10 m. Map background: shaded 30-m DEM from ASTER (a–d), 2015 SPOT images (e and f), or 2016 Pléiades images (g and h). [Color figure can be viewed at wileyonlinelibrary.com]

lower rhyolitic and the upper ones generally being granitic (Figure 4).

Above the kame terraces, the surface of the north side is covered by tills up to its top. To the west, a dense deposit of erratic boulders extends up to 2600 m asl (Figure 5b). Higher on the valley side, a few small moraines and kame terraces are distributed between *c.* 2650 and 2920 m (Figure 3), indicating at least three extents of the Kalguty Glacier larger than the one corresponding to the upper kame terrace and the terminal moraines at the west; two morainic crests located at 2750–2800 m on the east slope of the Klyuch valley, at the foot of the rock bump that culminates at 3020 m, could match the main moraine or the nearby small kame terrace on its west side (Figure 5c).

A second morainic complex crosses the Klyuch valley, reaching 2415 m asl at the confluence between the Kalguty and Ulan-Dawa Rivers. It mainly consists of six <2-m-high nested latero-frontal moraines, plus two or three very small ridges; the outermost frontal moraines are partly buried by alluvial deposits (Figure 5c). Several subparallel glacial lineaments highlighted by bushes, probably lateral moraines, are developed along the west side of the valley up to *c.*

2700 m, the two upper ones (with metre-size boulders) continuing the main kame terraces to the west. Slopes on both sides of the Klyuch valley are covered by tills, with abundant regolith and bedrock on the east side. Downstream from the Klyuch morainic complex, a set of small moraines is staggered along the gentle slope above the right bank of the river above 55 m, from the river confluence to Kalgutinskii Rudnik (Figure 5c). This *c.* 0.3-km^2 and 1.2-km-long area is up to 160 m high in Zone 3; the slope angle is *c.* 30° here, lower in the other zones (Figures 4 and 5d). Areas of scoured slabs of rhyolite with grooves, covered by rock coating and lichens, alternate with pieces of bedrock protruding above the soil surface; some trenches are several metres deep and wide, where frost weathering is very active.

Four other main morainic complexes are located in the downstream section of the lateral valleys on the Saylyugem side. Those in the Tundu-Uqgar and Central valleys have been mapped in detail (Figure 5d). The Tundu-Uqgar complex is formed by a large outermost latero-frontal moraine that develops down to 2480 m asl, and a dozen smaller nested recessional moraines – the largest ones lying on the right side, with the front of the innermost at 2620 m. Dozens of metre-sized erratic boulders are associated with the upper half of this morainic complex. The glacier tongue outside of the valley had an area of *c.* 2 km^2 when it built this complex. Outside the complex, tills cover the piedmont slopes, except along the bed of Ulan-Dawa River and its tributaries where alluvial deposits replace them. Inside the Tundu-Uqgar valley, no till seems to be present, as a consequence of reworking and deposition by post-glacial morphodynamics. The Central morainic complex consists of half a dozen moraines of various size, some with several crests; they are better preserved on the right side of the valley – the outermost, longest moraine is even absent on the left side (Figure 5d). The geometry and location of several moraines of this narrow complex indicate confluences with two small tributary glaciers flowing from the right side of the valley. The glacier front elevation oscillated from *c.* 2410 m (the remnant of the outermost moraine reaches 2435 m) to *c.* 2600 m, as suggested by the innermost recessional moraine crest.

We mapped the Argamji valley complex using satellite imagery only (Figure 5e). During the largest Argamji Glacier extent after separation from the smaller glacier from the East Argamji arm, its front was located at *c.* 2410 m. No moraine has been observed downstream from the confluence of the two glaciers, nor in the West valley (Figure 3). Finally, also incompletely surveyed, the East valley complex presents at least three latero-frontal moraines, the outermost reaching *c.* 2670 m; however, a larger left-lateral moraine suggests that a piedmont lobe could have reached the bottom of the Ulan-Dawa valley at *c.* 2600 m (Figure 5f).

Besides these downstream morainic complexes, smaller recent moraines are located at the head of several valleys on the south side of the basin. They have not been mapped in the East and Argamji valleys, where small glaciers are still present, owing to a lack of observations even by remote sensing. On the other hand, field observation on the cirque floor of the Central valley head has revealed two sets of probable moraines at 2850 and 3000 m for their lowest elevation, while possible right lateral moraines reach 3050 m (Figure 5g); the corresponding glacier front was probably bilobate. At the head of the Tundu-Uqgar valley, a 300-m-long morainic arc develops between 3000 and 3050 m, with *c.* 15- and 5-m-high distal and proximal sides, respectively (Figure 5h). Previous small glaciers in both valley heads were probably partly fed by snow avalanches detached from the *c.* 33°, 200- to 400-m-high slopes.

Reconstruction of the geometry of the palaeo Kalguty Glacier

The palaeo-glacier mainly indicated by the large West morainic complex was 23 km long, with a surface area of 157 km^2 (Figure 6). Its maximum thickness was *c.* 250 m at the present confluence of the Kalguty and Ulan-Dawa Rivers, and >200 m for the Tundu-Uqgar and Argamji arms. No ice cap covered the Teplyy Klyuch pass (2945 m asl) at that time, whereas some ice was likely to be flowing through the Ulan-Dawa pass (2695 m). Large glacierized cirques were present upstream from the Klyuch and Ulan-Dawa arms; right-lateral branches of the Central arm were fed from the Tundu-Uqgar arm, while many small cirque and valley glaciers contributed to the Argamji arm.

Geochronological results

SED data treatment

Eleven ages were obtained on bedrock ($n = 9$) and overlying erratic boulders ($n = 2$). ^{10}Be ages range from 18.91 to 23.56 ka, and corresponding ^{26}Al ages range from 13.49 to 18.59 ka (Table 3). Ages computed with the Lm scaling are 4.6% older than with the LSDn scaling (Table 3), which does not affect our interpretation. There is a significant discrepancy between the ^{10}Be and ^{26}Al datasets, as only three samples yield similar ^{10}Be and ^{26}Al ages and have ^{26}Al/^{10}Be ratios close to the canonical value of 6.75 (Balco et al., 2008; Fenton et al., 2022; Table 2) – although this value could vary slightly with altitude and latitude (Corbett et al., 2016a). All other samples have lower ^{26}Al/^{10}Be ratios and younger ^{26}Al ages. Such a discrepancy can arise either from problems during chemical processing of the samples in the laboratory (e.g. Ruszkiczay-Rüdiger et al., 2021) or from a complex exposure/burial history involving non-erosive cold-based ice (e.g. Corbett et al., 2016b). Drawing on that, it is not possible to average dating results obtained with the two nuclides. Based on ^{26}Al/^{10}Be ratios, we can distinguish two groups in a first approximation as shown in Figure 7A, where the ellipses represent one sigma envelopes. Samples from the lowest group (Z2R and Z3B) that do not overlap at one sigma with the other were considered as outliers. We discarded those two samples that displayed very low ratios and also yielded the two oldest ^{10}Be ages, as they probably contain nuclides inherited from a prior period of exposure. One of the erratic samples (Z2B) was kept for exposure age calculation as it cannot be treated as an outlier based on ^{26}Al/^{10}Be ratio. However, it is significantly older than the dated bedrock surface on which it rests. Finally, we chose to base our chronology of the deglaciation only on the ^{10}Be ages, as laboratory procedures and production rates are better constrained for this widely used nuclide. We also stress here that ^{10}Be ages conform better to the stratigraphy than ^{26}Al ages. Lateglacial ages are not expected at this location, while all ^{26}Al ages fall into that time period.

Age of Kalgutinskii Rudnik deglaciation and of the Kalguty stage

Erratic boulders and glacially polished bedrock track the glacier position during a deglaciation sequence. The arithmetic mean of ^{10}Be exposure ages shows that Kalgutinskii Rudnik was deglaciated at *c.* 20.7 ± 1.1 ka (Figure 7B). As mentioned above, no snow or erosion correction has been applied, which means that these ages are minimal.

The surface of Kalguty Glacier was probably *c.* 50–60 m higher than the top of the *roches moutonnées* when it built the West morainic complex, as suggest by the kame terrace (Figure 8C) and our reconstruction of surface topography of the glacier during the

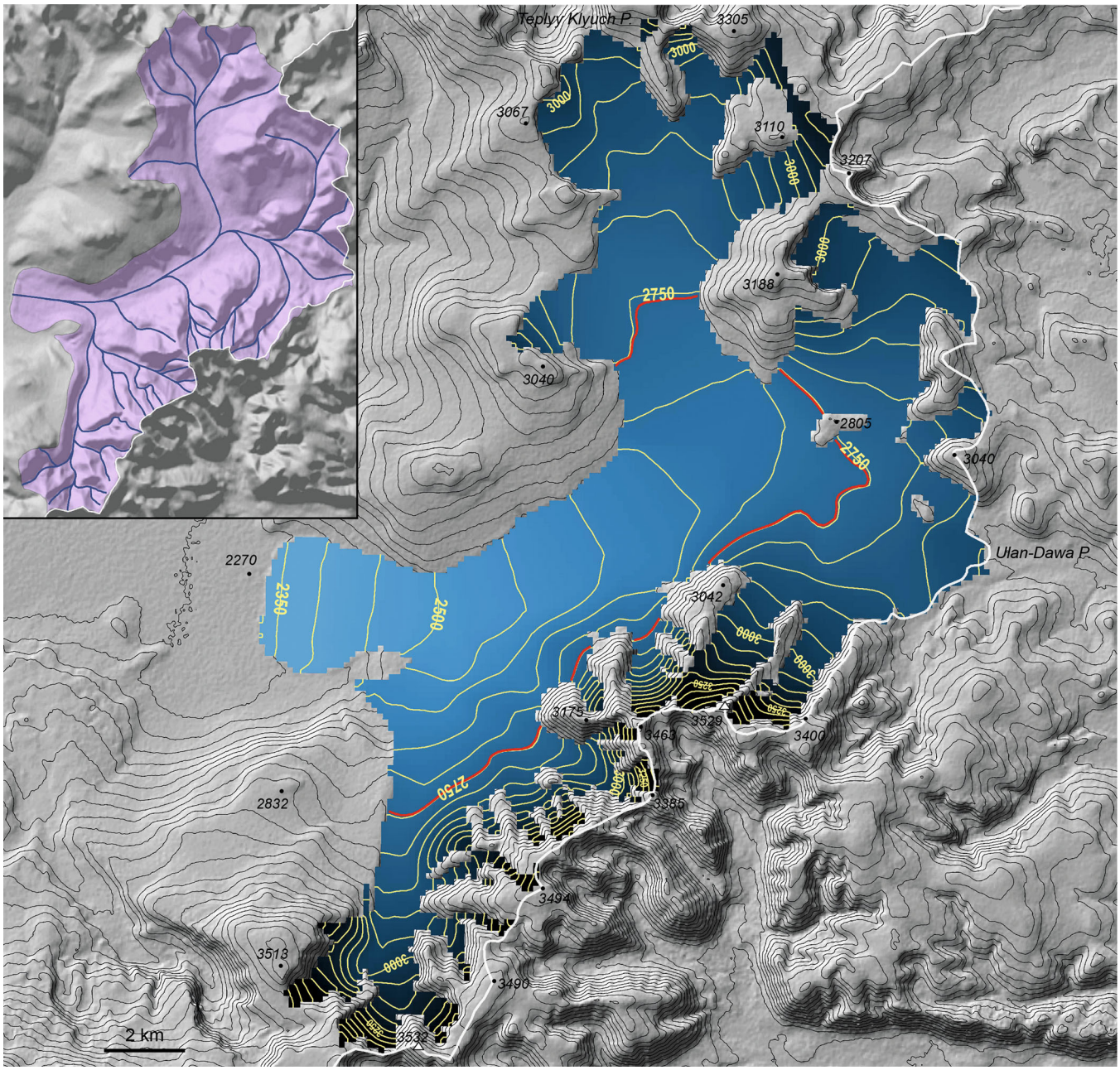

Figure 6. Reconstruction of the extent and surface topography of the glacier during the Kalguty stage. Red line: equilibrium-line altitude; white line: boundary between Russia and Mongolia. Contour line interval: 50 m. Map background: shaded 30-m DEM from ASTER. Reconstruction from *GlaRe* toolbox (Pelitero et al., 2016): blue lines and purple area in the inset map are *GlaRe* flowlines and watershed, respectively. [Color figure can be viewed at wileyonlinelibrary.com]

Table 3. Surface exposure ages from the petroglyph site Kalgutinskii Rudnik. The two outliers are in italic type.

Sample	^{10}Be age LSDn (ka)	Int. unc. (ka)	Ext. unc. (ka)	^{10}Be age Lm (ka)	Int. unc. (ka)	Ext. unc. (ka)	^{26}Al age LSDn (ka)	Int. unc. (ka)	Ext. unc. (ka)	^{26}Al age Lm (ka)	Int. unc. (ka)	Ext. unc. (ka)
Z1Q1	20.71	0.78	1.74	21.57	0.84	1.87	17.07	0.54	1.82	17.99	0.57	1.79
Z1Q2	20.02	0.61	1.59	20.84	0.65	1.73	18.35	0.66	2.03	19.36	0.71	1.94
Z1B	—	—	—	—	—	—	—	—	—	—	—	—
Z1R	20.42	0.93	1.77	21.27	1.00	1.92	16.20	0.85	1.93	17.05	0.91	1.84
Z2Q1	20.32	0.62	1.62	21.21	0.66	1.76	17.41	0.53	1.93	18.38	0.58	1.82
Z2Q2	20.47	0.78	1.69	21.37	0.84	1.85	18.26	0.63	1.99	19.29	0.67	1.92
Z2B	22.24	0.85	1.89	23.27	0.90	2.02	17.57	0.65	1.89	18.56	0.69	1.87
Z2R	*22.39*	*0.97*	*1.97*	*23.43*	*1.02*	*2.09*	*14.18*	*0.70*	*1.62*	*14.93*	*0.76*	*1.59*
Z3Q1	20.41	0.64	1.66	21.41	0.69	1.79	17.55	0.71	1.97	18.62	0.78	1.91
Z3Q2	22.54	1.18	2.08	23.72	1.24	2.22	17.22	0.60	1.86	18.27	0.63	1.82
Z3B	*23.56*	*0.79*	*1.97*	*24.79*	*0.84*	*2.10*	*13.49*	*0.44*	*1.49*	*14.25*	*0.48*	*1.41*
Z3R	18.91	0.90	1.69	19.81	0.95	1.79	18.59	1.06	2.22	19.74	1.17	2.17

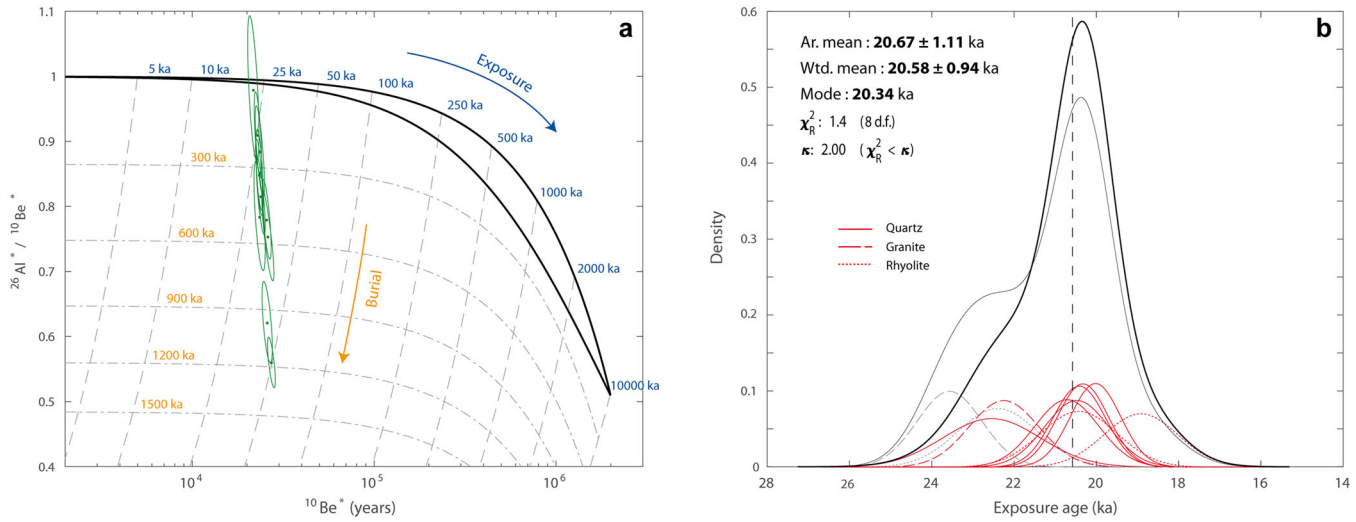

Figure 7. (a) ^{26}Al–^{10}Be 'banana plot' computed with the *iceTEA* tool (http://ice-tea.org; Jones et al., 2019) with the LSDn scaling model (Lifton, 2014). Ellipses show one sigma envelopes. Samples from the lowest group do not overlap at one sigma and are considered as outliers. (b) normal kernel density estimate for ^{10}Be ages of bedrock (rhyolite and quartz) and erratic boulders (granite) at Kalgutinskii Rudnik (the two outliers are shown in grey). Summed probabilities are displayed for all samples without the two outliers (thick curve) and for all samples (thin curve). [Color figure can be viewed at wileyonlinelibrary.com]

Kalguty stage (Figure 6). We estimate the linear thinning rate of the glacier at Kalgutinskii Rudnik using the *iceTEA* tool (Jones et al., 2019). It yields a mean thinning rate of 0.18 m a^{-1} for the glacier surface along the 150-m-high *roches moutonnées* (Figure 8B). This suggests that the age of the West morainic complex is >21 ka, corresponding to the Kalguty stage, probably the maximum extent of the Kalguty Glacier during MIS 2.

The two erratic boulders Z2B and Z3B have a significantly higher ^{10}Be surface concentration than that of the bedrock, as observed elsewhere (e.g. Delmas et al., 2011). Indeed, either with or without outlier removal, boulder age (arithmetic mean: 22.4 ± 0.9 or 22.9 ± 0.9 ka) is *c.* 2 ka older than underlying bedrock age (arithmetic mean: 20.5 ± 1.0 or 20.7 ± 1.1 ka), which could indicate that any inherited nuclides from a previous period of exposure has been effectively removed from bedrock surface during the last glaciation. As granite outcrops only 7.5 km upstream, we can discard inheritance acquired by supraglacial transport. Based on a large dataset of glacial boulder ^{10}Be exposure ages, Heyman et al. (2011) showed that incomplete exposure is more frequent than prior exposure, and stated that the maximum apparent exposure age of glacial boulders should be viewed as a minimum deglaciation age. Although their height is <1.6 m (Table 1; Heyman et al., 2016), the boulders are not rooted in sediments but resting on bedrock (Figure 4), suggesting that they were not prone to shielding from cosmic rays since deposition.

On the other hand, the *roches moutonnées* at Kalgutinskii Rudnik could have been buried by till for some time, and by a thin snow cover. Prud'homme et al. (2020) suggested that apparent exposure ages in erratic boulders and polished bedrock should be considered as maximum and minimum ages of glacial retreat, respectively. As we discarded the two oldest ages based on discordant ^{26}Al data, the remaining oldest age of *c.* 22.5 ka for the bedrock (Z3Q2) could be considered as a minimum age for the West morainic complex and therefore the Kalguty Stage corresponding to the MIS 2 maximum.

Lateglacial stages in the upper Kalguty basin

Two Lateglacial (Lg) stillstands have been reconstructed with *GlaRe* (Figure 9). Due to lack of field and remote-sensing observations, Lg1 was not reconstructed for the cirques north of the Ulan-Dawa River, nor Lg2 for Argamji and East Argamji Glaciers. Lg1 for East Glacier was manually reconstructed, based on tenuous lineaments on satellite images, which may be moraines. Other limits or flaws in our *GlaRe* reconstruction are: (i) few or no change between Kalguty Stage and Lg stillstands in the upper area of the valleys; (ii) small cirques on the south side of East Argamji not considered; and (iii) glacier areas missing for Kalguty Stage and Lg stillstands in East and Argamji valley heads although present during the LIA (see Fig. S2).

The few moraines located in the main valley upstream from the West complex (downstream from the Argamji mouth and the Klyuch complex: Figure 5b and c, respectively) and the numerous recessional moraines in the Klyuch, Tundu-Uqgar and Central valleys (Figure 5c and d) between the extent of Lg1 and Lg2 suggest that the glaciers retreated to the tributary valleys throughout the Lateglacial.

Lg1 glaciers (incomplete) covered an area of 65.6 km^2, of which 45% was the Klyuch Glacier, and Lg2 glaciers (very incomplete) covered 32.5 km^2 (Table S1). Maximum thickness was 200 m for Klyuch and Argamji Glaciers during Lg1, and >100 m for Tundu-Uqgar Glacier during Lg1 and 2.

ELA of the Kalguty, Lateglacial and LIA stages

Values for reconstructed ELA with the AAR and AABR methods are very close for the four stages Kalguty, Lg1 and 2 (Lateglacial), and LIA (LIA extent: Figs S1 and S2). ELA depression with respect to the LIA ELA value is *c.* 500, *c.* 400 and 315 m for the Kalguty stage, Lg1 and 2, respectively (Table 4).

Discussion

Maximum extent of glaciers in the Altai mountains during MIS 2

Patterns of Pleistocene glaciation in the Russian Altai Mountains are still debated in both time and space (Herget et al., 2020). On his map of the Pleistocene glaciations in the south-eastern Russian Altai region, Deviatkin (1965, in Herget, 2005: fig. 21) considered that the West Kalguty morainic complex corresponds to the 'first post-maximum glaciation in Upper Pleistocene', whereas the Argamji moraine complex marks the extension of the second one. By contrast, authors studying the Russian Altai Mountains and their

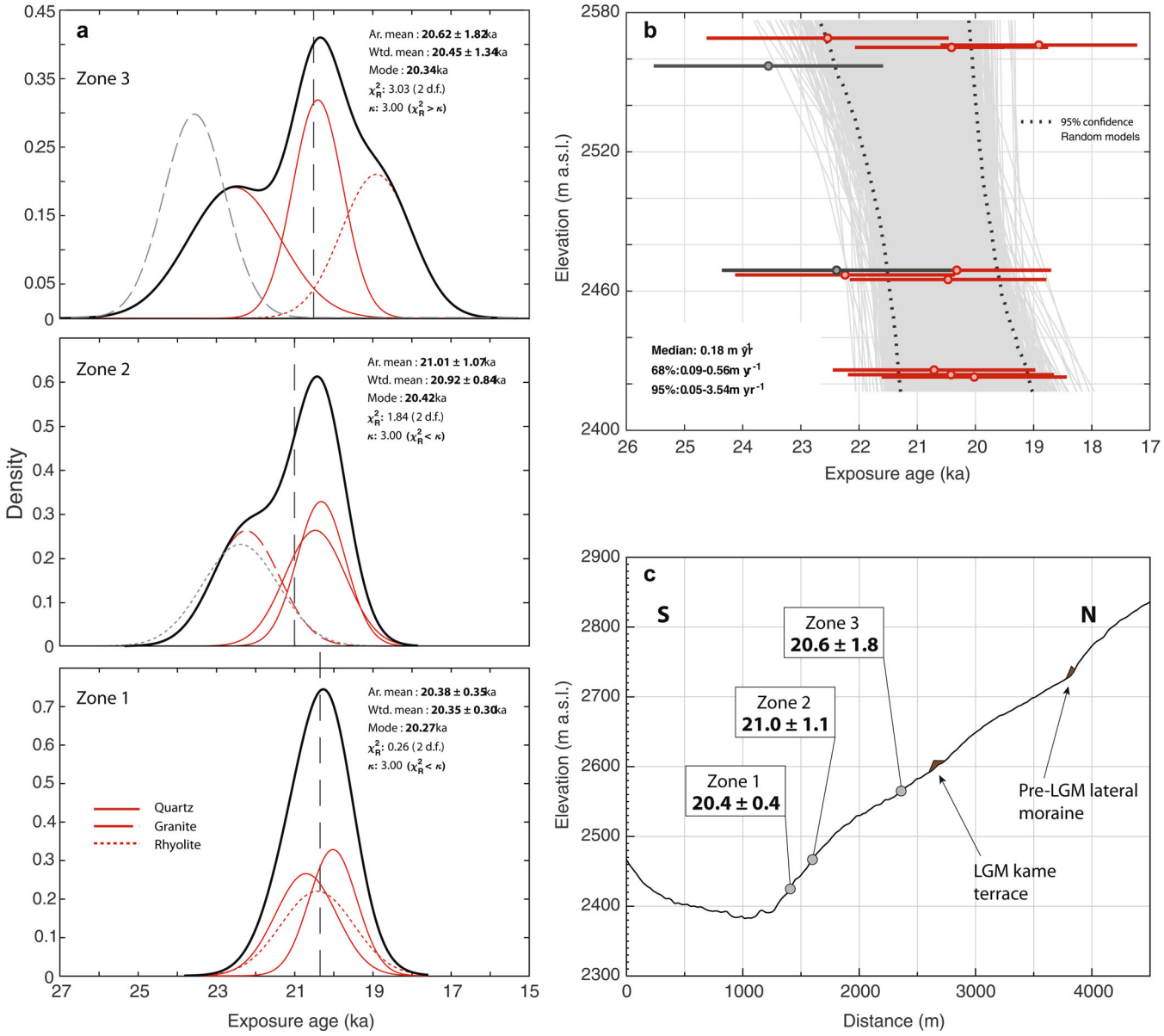

Figure 8. (a) normal kernel density estimate for ^{10}Be ages as distributed in the three zones of Kalgutinskii Rudnik (summed probability: black curve). (b) vertical transect recording glacier surface lowering computed with the *iceTEA* tool (Jones et al., 2019) using unweighted least square regression (the two outliers are shown in grey). (c) cross-section of the Kalgutinskii Rudnik hillslope with exposure age arithmetic mean shown for each zone (cross-section location on Figure 3; zone location on Figure 4). [Color figure can be viewed at wileyonlinelibrary.com]

glaciations at a regional scale in the 1980s–1990s generally considered that the entire Russian Altai Mountains except the Chuya basin were ice-covered during the Late Pleistocene/LGM (e.g. Kotljakov et al., 1997). Still at a regional scale, Lehmkuhl et al. (2011: fig. 69.5) mapped their LGM extent on the entire Kalguty basin, without considering the West morainic complex. Blomdin et al. (2016) mapped the Argamji and East Argamji terminal moraines and the West morainic complex, while the Tavan Bogd ice cap on their 'Minimum extent of maximum glaciation' covers the upper Kalguty – but not its north side or the Klyuch Glacier.

Estimates of worldwide ice volume since 35 ka from sea-level reconstruction shows a rapid ice growth at 31–29 ka, an ice-volume peak at *c.* 20.5 ka, followed by a deglaciation accelerating from 16.5 ka (Lambeck et al., 2014). Therefore, the global LGM, that is the period with global maximum ice volume during the last glacial cycle between 110.8 and 11.7 ka (Hughes et al., 2013), took place during MIS 2. Depending on studies, the onset and end of the global LGM vary from 27.2 to 23.0 ka and from 23.0 to 19.0 ka, respectively (Sanchez Goñi and Harrison, 2010: Table 2), around the classically global LGM defined at 26.5–19 ka by Clark et al. (2009).

However, many mountain glaciers were at their MIS 2 maximum at the beginning of the stage when ice sheets had only started to grow (Clark et al., 2009). Moreover, while the extent of the Laurentide or Alpine Ice Sheets for instance was maximal close to the global LGM during MIS 2 – with great impact on global sea level – a majority of glaciers in Asia or New Zealand mountains, or the East Antarctica Ice Sheet reached their maximum during MIS 3, 4 or 5 (Hughes et al., 2013). The Kalguty stage, close to the global LGM, appears to show the greatest glacier extent in the upper Kalguty basin during MIS 2.

The number of studies focusing on glacier extent during MIS 2 in the Altai region has increased in recent years (Figure 10). Damming of the Kuray and Chuya basins (Russia; Figure 1) by glaciers, flowing during the Late Pleistocene from the North Chuya Range and the north side of the basins, have long been hypothesized (e.g. V. A. Obruchev in 1914). The deep and wide glacial lakes drained repeatedly, paced by glacier

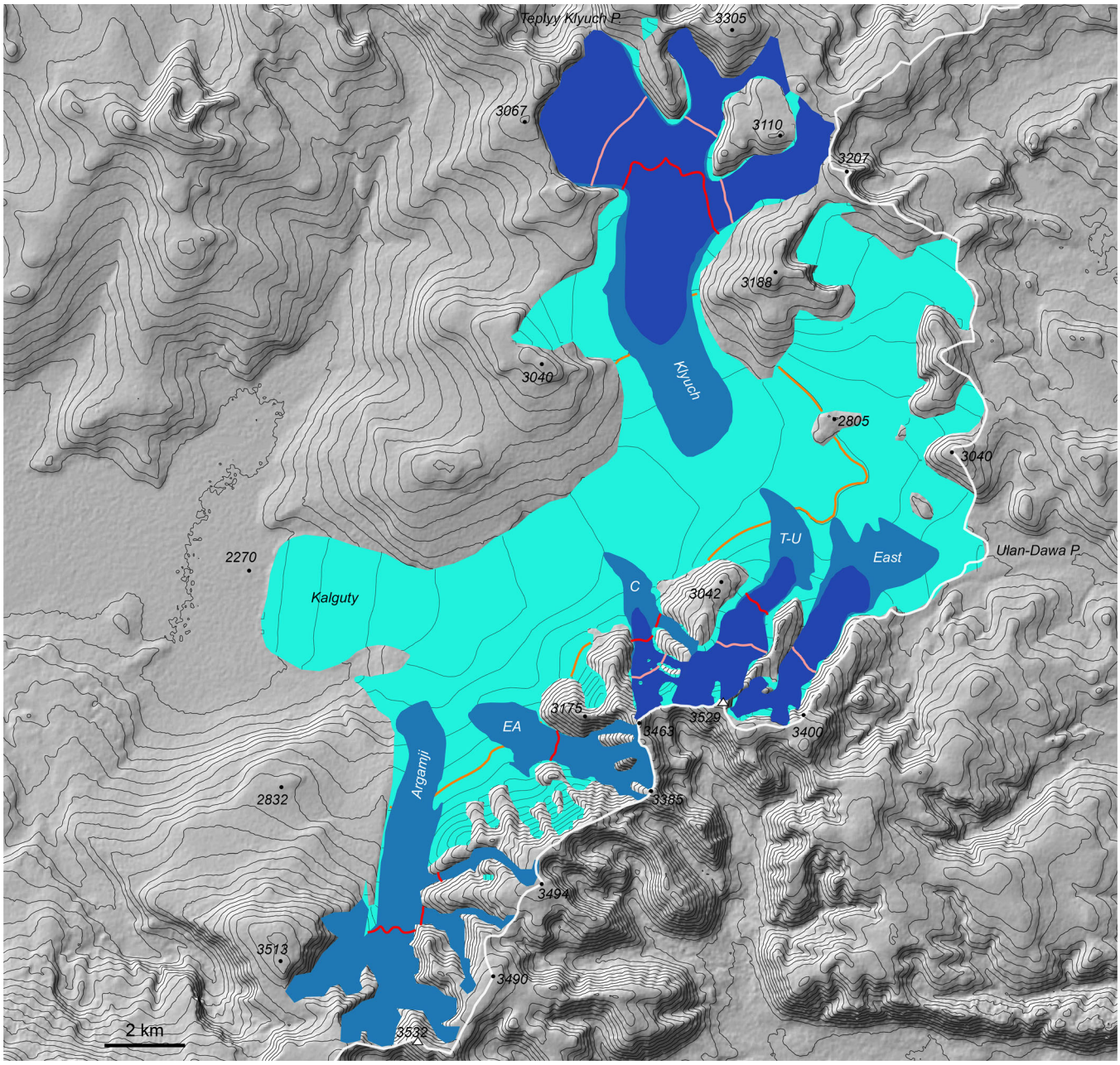

Figure 9. Reconstruction of pre-Holocene glacier stillstands and their equilibrium-line altitude (ELA) in the upper Kalguty. Cyan: Kalguty Stage (MIS 2); light blue: Lateglacial 1 (Lg1); dark blue: Lateglacial 2 (Lg2). Orange, red and pink lines: respective ELAs. EA: East Argamji; C: Central; T-U: Tundu-Uqgar. Geometry of glaciers from *GlaRe* toolbox was adjusted to the topography of cirques and crests in the valley heads. Contour line interval: 50 m. Map background: shaded 30-m DEM from ASTER. [Color figure can be viewed at wileyonlinelibrary.com]

Table 4. Reconstructed ELA of Kalguty (MIS 2), Lg1 and Lg2 (Lateglacial), and LIA stages, and their ELA depression with respect to the LIA values (ΔELA^{LIA}; m asl).

	Kalguty stage			Lg1		Lg2		LIA	
Glacier	AAR 0.6	*AABR 1.75*	Glaciers	AAR 0.6	*AABR 1.75*	AAR 0.6	*AABR 1.75*	AAR 0.6	*AABR 1.75*
Kalguty	**2747**	***2727***	Argamji	2917	*2917*	?	*?*	3268	*3266*
			East Argamji	2783	*2843*	?	*?*	—	—
			Tundu-Uqgar	2847	*2907*	3017	*2997*	3268	*3261*
			Central	2741	*2781*	2920	*2920*	3086	*3106*
			Klyuch	2780	*2760*	2808	*2808*	—	—
			East Valley	?	*?*	2939	*2959*	3236	*3236*
			Weighted mean	**2814**	***2842***	**2921**	***2921***	**3235**	***3236***
ΔELA^{LIA}	**488**	***509***		**421**	***394***	**314**	***315***	**0**	***0***

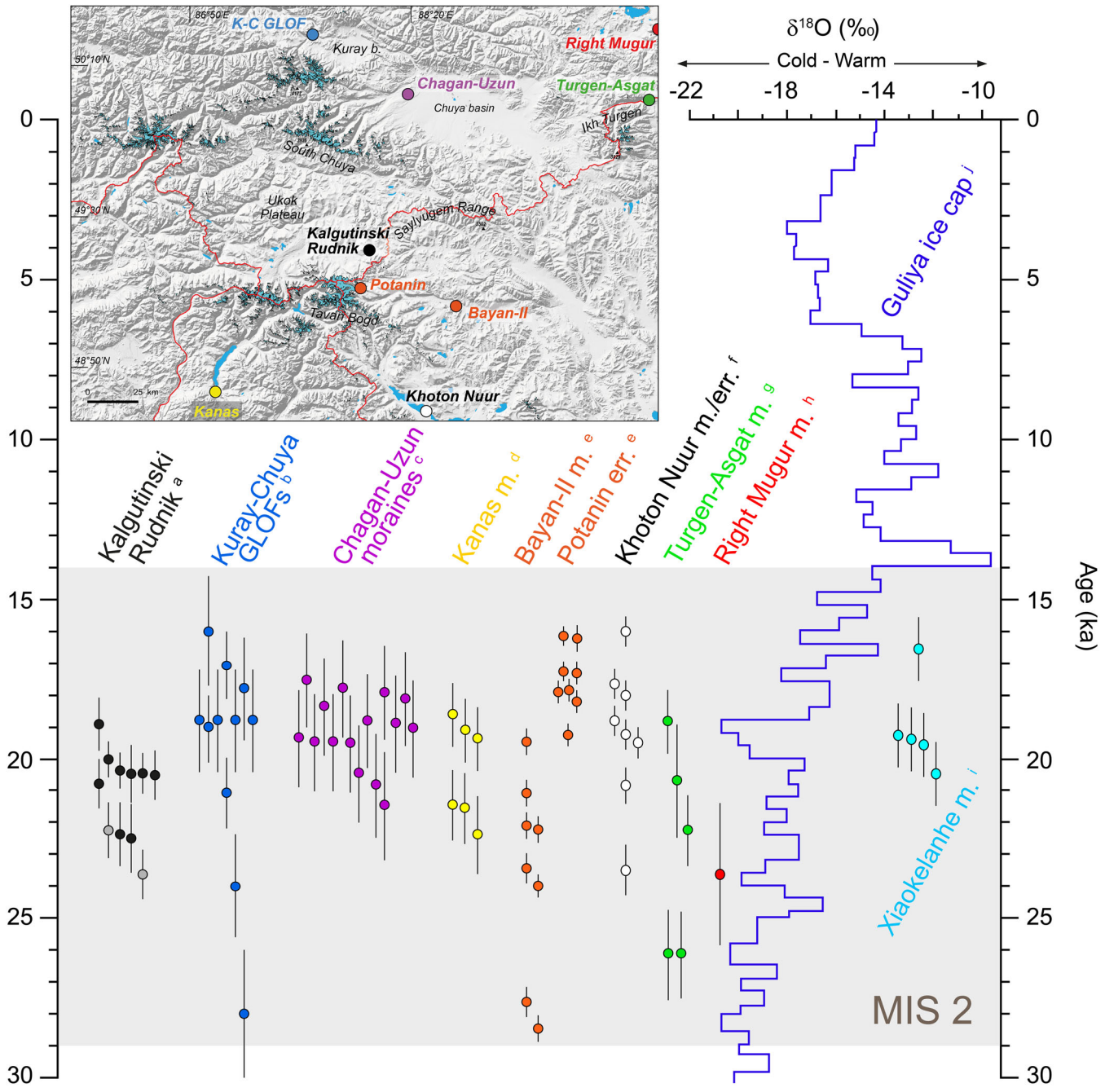

Figure 10. Distribution of ages of *roches moutonnées*, glacial lake outburst floods (GLOFs), moraines (m.) and erratics (err.) in the Altai Mountains during MIS 2 (29–14 ka; Martinson et al., 1987), related to temperature change in Tibet (Guliya Ice Cap). (a) this study (grey dots: outliers); (b) Reuther et al., 2006; Agatova et al., 2020; Herget et al., 2020; (c) Gribenski et al., 2016; (d) Gribenski et al., 2018; (e) Radue, 2018; (f) Strand et al., 2022 [arithmetic mean (three to nine samples) for five moraines and three erratic sets]; (g) Blomdin et al., 2018; (h) Ganyuskin et al., 2018a; (i) Dong et al., 2020 (outside the location map); (j) Thompson et al., 2005. Ages of the moraines and erratic boulders are mostly from SED, while GLOF ages resulted from different dating methods: SED on flood-associated boulders, OSL dating on flood and lacustrine deposits and radiocarbon dating on subaerial deposits. Blue areas on location map: present-day glacier extent according to RGI 6.0 (RGI Consortium, 2017). [Color figure can be viewed at wileyonlinelibrary.com]

fluctuations. Landforms resulting from glacial lake outburst floods (GLOFs) have been extensively studied, and peak discharge has been modelled (Baker et al., 1993; Rudoy, 2002; Herget, 2005; Carling et al., 2011). Dating by Reuther et al. (2006), recently taken up and completed by Gribenski et al. (2016), Agatova et al. (2020) and Herget et al. (2020), suggests at least three GLOFs probably triggered by glacier shrinkage slightly before 24.0 ± 1.6 and 21.1 ± 1.2 ka, and at 18.7 ± 1.6 ka, and possibly two GLOFs slightly before 28.0 ± 2.0 and at 16 ± 1.7 ka (Figure 10) – although these ages and their interpretation remain of debate, especially since they resulted from different dating methods and controversial interpretations of field evidence (Herget et al., 2020).

At the west end of the Chuya basin, mean ages obtained from SED of 15 samples on the Chagan-Uzun glacial complex range from 19.7 ± 1.2 to 18.5 ± 0.8 ka (Figure 10). Extending over a distance of 17 km between 1876 and 2399 m asl, these close ages indicate surge-like glacier dynamics building the outermost moraine followed by a retreating period with short stillstands and readvances, as suggested by the landform–sediment associations (Gribenski et al., 2016). However, the outermost moraine age (19.2 ± 1.8 ka) is underestimated as the moraine was covered by several tens of metres of water for an unknown duration, as shown by Chuya Lake shorelines up to *c.* 2100 m (Carling et al., 2011). Herget et al. (2017) document that Chagan-Uzun glaciers reached farther downstream than

the terminal moraine assumed to represent the MIS 2 last maximum extent at that location (Gribenski et al., 2016).

The 4-km-long and 3-km-wide Kanas Lake morainic complex (China) is located at *c.* 1400 m asl, 90 km downstream from the summit of the Tavan Bogd Massif, at the outlet of a basin whose glacier surface area was still *c.* 210 km^2 in 1980 (Zhao et al., 2013; Figure 10). Besides about 15 5- to 10-m-high frontal moraines, the complex comprises kame terraces and meltwater channels, and continues downstream with hummocky terrain and an outwash plain. Optically stimulated luminescence (OSL) dating has suggested that deposition was mainly during MIS 3 (Xu et al., 2009; Zhao et al., 2013), but recent SED gives six ages ranging from 22.4 ± 1.3 to 18.7 ± 1.1 ka, distributed in outer glacier retreat and inner glacier advance sets with mean ages of 21.8 ± 0.5 and 19.1 ± 0.4 ka, respectively (Figure 10; Gribenski et al., 2018). Two infrared stimulated luminescence ages agree within error with the SED ages, at 23.5 ± 6.1 and 27.4 ± 4.9 ka, while also suggesting that the SED ages could be underestimated as no erosion correction was applied (Gribenski et al., 2018).

In the valley head of the *c.* 100-km-long, deeply carved Tsagaan Gol valley (Mongolia), the Potanin Glacier flows from the Tavan Bogd icefield to reach 2915 m asl (Figure 10). Joined by the Alexandra Glacier in its distal section, their total surface area was 37 km^2 in 2011 according to RGI 6.0, while 30 other smaller glaciers are still present in the Tsagaan Gol basin (Ganyuskin et al., 2018b). While the Potanin front has retreated by 2.5 km since the LIA (Ganyuskin et al., 2018b), a 4-km-wide morainic complex is located 57 km downstream from the present front, between 2150 and 2250 m asl, and is continued downstream with a 30-km-long outwash plain. Many small and discontinuous frontal moraines and a few rare moraines up to 40 m high form this complex, in which two morainic units have been studied: Bayan I dated at 54.0 ± 2.8 ka and Bayan II (Figure 10) whose eight ages range from 28.5 ± 0.4 to 19.5 ± 0.4 ka, with possible stages at *c.* 28.0, 23.0 and 20.5 ka (Radue, 2018).

Surrounding the Khoton Nuur (Mongolia), a 21-km-long lake, a wide morainic complex is composed of four sets of moraines attributed to the last glacial cycle (Figure 10). While the outermost Khoton Moraine IV is attributed to MIS 3 (35.4 ± 1.0 ka), arithmetic mean ages of Khoton Moraines III, II and I are 23.4 ± 0.8, 20.8 ± 0.6 and 19.5 ± 0.5 ka, respectively; erratic boulders were then deposited until 18.1 ± 0.5 ka during the Khoton Glacier recession, before its re-advance at 17.7 ± 0.5 ka (Figure 10; Strand et al., 2022).

At the outlet of the 30-km-long, U-shaped Turgen-Asgat valley (Ikh Turgen massif, 3896 m asl, Russia–Mongolia), a 6-km-wide bilobate morainic complex extends between 2300 and 2000 m asl (Figure 10); its numerous lateral moraines dominate the Mogen-Buren piedmont plain by 150 m. Five granitic boulders have been sampled on the innermost right-lateral moraine, whose ages range from 26.2 ± 1.7 to 18.7 ± 1.2 ka, with a mean age of 22.8 ± 3.5 ka (Figure 10; Blomdin et al., 2018). Other MIS 2 ages have been obtained from the Boguty morainic complex, on the south-west side of the massif, but they are entangled with older ages (Blomdin et al., 2018).

Culminating at 3971 m asl, the Mongun-Taiga massif (Russia) still has a glaciated area of 20 km^2, mainly in its north-est sector where glacial landforms and deposits have been recently investigated in four valleys, including the Right Mugur valley (Figure 10). Ganyuskin et al. (2018a) recognized three stages in their morainic complexes that extend over a distance of 7 km from 2400 to 3200 m asl. Based on geomorphology and stratigraphy, and radiocarbon ages from buried wood material, peat and soil, they hypothesized their correspondence with MIS 4, MIS 2 and the Neoglacial. However, the unique MIS 2 ^{10}Be age (23.6 ± 2.3 ka; Figure 10) results from an outermost end-moraine of the Right Mugur Glacier considered to be of MIS 4, whereas a second ^{10}Be age from this moraine is 11.2 ± 1.1 ka. Discussing this contradiction, Ganyuskin et al. (2018a) consider that boulder exhumation is more probable than an MIS 2 age for the outermost moraines.

Finally, Dong et al. (2020) documented two sets of moraines at the head of the no longer glacierized Xiaokelanhe basin (3200 m asl, China), 125 km south-east of the upper Kalguty basin. While the terminal moraine mean age is apparently 34.1 ± 5.0 ka, five samples (including one outlier) on the innermost latero-frontal moraine *c.* 0.5 km upstream at 2380 m asl gave an arithmetic mean age of 19.7 ± 0.5 ka (Figure 10).

Therefore, the Kalguty Stage minimum age of 21 or 22.5 ka could match with (i) a glacier retreat suggested by Kuray-Chuya GLOFs at *c.* 24.0 or 21.1 ka, (ii) a Chagan-Uzun Glacier advance prior to 19.2 ka, (iii) a Kanas Glacier retreat at *c.* 22.0 ka, (iv) Tsagaan-Gol Glacier advances at 23.0 and 20.5 ka, (v) Khoton Glacier advances at 23.4 and 20.8 ka, (vi) a Turgen-Asgat Glacier advance around 22.8 ka, and even with (vii) a possible Right Mugur Glacier advance around 23.6 ka (Figure 10).

The smooth topography of the north side of the upper Kalguty valley covered by till, and probably a short lateral moraine and a few small kame terraces lying on it in the range 2680–2750 m asl (Figure 3) suggest a more extended glacier prior to the Kalguty Stage. The valley extends 20 km from the West morainic complex, with a 5-km-wide alluvial plain, and has probably been carved during previous glaciations, when a large ice mass was flowing from the north side of the Tavan Bogd Massif (Figs. 2 and S3). Few studies suggest that maximum glacier extent during the last glacial cycle in the Altai mountains occurred at the beginning of MIS 2 (Herget et al., 2017) – the Tsagaan Gol-Potanin Glacier would have first reached the Bayan-II moraines at *c.* 28 ka (Figure 10; Radue, 2018) – although some of their dating results are discussed (Gribenski et al., 2017). Other studies place the local LGM earlier than MIS 2, due to wetter conditions (Herget et al., 2020, and references therein), generally during MIS 4 – for example 69–63 ka in the nearby Kanas valley (Gribenski et al., 2018), or as hypothesized by Ganyuskin et al. (2018a) for the Mongun-Taiga massif. While a re-evaluation of glacial chronologies in the Central Asia concluded that there was no significant ice expansion during MIS 3 (59–29 ka; Gribenski et al., 2018, and references therein), as already suggest by Lehmkuhl et al. (2016) for the Mongolian Altai, few studies document a major glacier advance during MIS 3 in the Altai Mountains: a Turgen-Asgat moraine in drier Ikh Turgen Mountains is dated to *c.* 45 ka (Blomdin et al., 2018), the outermost one of the Khoton Nuur complex is dated to 35.4 ka (Strand et al., 2022), while Dong et al. (2020) propose a local LGM at 34.1 ka in the Xiaokelanhe River basin.

Glaciers in the Altai Mountains during the Lateglacial (<19 ka)

Few Lateglacial stillstands have been recognized in the Altai Mountains up to now. Blomdin et al. (2016) mapped on their 1:1000 000 map as 'glacier valley' – without any chronology – similar extents to our upper Kalguty Lg1 or Lg2 extents, whereas Chuya and Kuray GLOFs at 18.7 ± 1.6 ka and possibly at 16.0 ± 1.7 ka (Figure 10) could correspond to Lateglacial retreat stages.

About 200 m above the LIA proglacial margin of the Potanin Glacier, eight erratic boulders aligned between 3034 and

3013 m asl on the left side of the Tsagaan Gol valley were sampled by Radue (2018), and the ages of these boulders range from 19.3 ± 0.3 to 16.1 ± 0.2 ka (Figure 10). Their mean age of 17.5 ± 0.5 ka indicates a probable stagnant or retreating phase of the glacier during the Lateglacial. A cluster of three erratic boulders located 19 km downstream from the present Potanin front at *c.* 2600 m, that geometrically fits with the same glacier stillstand, have been dated from 17.1 ± 0.3 to 15.9 ± 0.4 ka (Radue, 2018).

While three sets of erratic boulders inside the Khoton Nuur morainic complex, with mean ages from 19.3 ± 0.5 ka downstream to 18.1 ± 0.5 ka upstream, attest to glacier shrinkage after 19.5 ± 0.5 ka (Khoton Moraine I), the glacier re-advanced at 17.7 ± 0.5 ka (Tsagaan-Sol Moraine I) and 16.0 ± 0.5 ka (Takhilt Valley Moraine I; Figure 10), respectively *c.* 32 and 54 km upstream of Khoton Moraine I (Strand et al., 2022).

In the East Mugur valley (Mongun-Taiga massif), three of five nested latero-frontal moraines ranging from 2600 to 2800 m asl along a distance of 4 km are attributed to Lateglacial stages, between *c.* 14 and 12 ka (Ganyuskin et al., 2018a; MIS 2 stages 3–5 on Figure 5).

By analogy with these Altai Lateglacial stages, Lg1 and Lg2 stillstands in the upper Kalguty basin could have taken place: (i) around 17.5 and 16 ka, like the Khoton Glacier which had lost at that time 50 and 90% of its MIS 2 maximal length, respectively (Strand et al., 2022), the Potanin Glacier at 17.5 ka (Radue, 2018) or a Kuray GLOF at 16.0 ka (Herget et al., 2020); (ii) immediately after the termination of MIS 2, between *c.* 14 and 12 ka, in correspondence with 'MIS 2 stages 3, 4 and 5' defined by Ganyuskin et al. (2018a) for the Mongun-Taiga massif – with close ELAs (cf. section 4.3).

ELAs in the Altai Mountains since MIS 2

Comparing ELA values of the present Altai glaciers is not reliable as their sources are heterogeneous (mean values for a whole area or even a range based on observation of individual glaciers, or on regional modelling, and for different periods). For instance, a mean ELA of 3390 m asl (3335 m asl) on the north side of Tavan Bogd Massif in 2010 (2015) resulted from 16 observed glacier ELAs ranging from 3110 to 3695 m (Ganyushkin et al., 2017; 2018b). Lehmkuhl et al. (2011) proposed a mean ELA of 3400 m too but for the entire Tavan Bogd Massif, for which Ganyushkin et al. (2018b, 2022) calculated a mean ELA of 3285 and 3358 m in 2010 and 2006–2020, respectively.

The weighted mean value for our reconstructed LIA ELA in the upper Kalguty basin is 3235 m asl (Table 4), close to the mean value of 3275 m given by Ganyushkin et al. (2015). The Kalguty MIS 2 ELA at *c.* 2750 m is close to the values of the nearby Tsagaan Gol-Potanin and the more distant Mongun-Taiga, and to the value of 2735 m for the Tavan Bogd north side proposed by Moskalenko et al. (2013) but their LIA ELA is 180 m lower than proposed by Ganyushkin et al. (2018b). The variability of the MIS 2 ELAs in Altai (*c.* 350 m) is slightly higher than the present one (*c.* 200 m). On the other hand, the Kalguty ELA depression compared to the present ELA (ΔELA^{pr}) is quite different from those of all ranges excepted in the Mongun-Taiga (Table 5).

These MIS 2 values in the continental Altai Mountains are very different from those of the wet European Alps, where ELA ranged from <1100 m (north side) to >1500 m asl (west side; Kuhlemann et al., 2008); Alpine ΔELA^{pr} values are two to three times higher than Altai ones, from 1055 m (Gesso Glacier; Federici et al., 2017) and 1150 m (Julian Prealps; Monegato, 2012) to 1300–1500 m for the large valleys of Durance, Susa and Aosta (Ivy-Ochs et al., 2018) – though Serra et al. (2022) suggest for the last an MIS 2 ELA and a ΔELA^{pr} of *c.* 2300 m and *c.* 570 m, respectively.

The ELA depression compared to the LIA ELA (ΔELA^{LIA}) for Lateglacial stages Lg1 and Lg2 of the upper Kalguty basin has been reconstructed at 421 and 314 m, respectively (Table 4). Using the value of 3374 m for the present ELA (Table 5; Ganyuskin et al., 2018b) results in a ΔELA^{pr} of 560 and 453 m for Lg1 and Lg2, respectively. There has been no reconstruction of ELA and ΔELA for Lateglacial stages in the Altai Mountains, except for the East Mugur valley (Mongun-Taiga massif), where Ganyuskin et al. (2018a) suggest an ELA depression compared to the present ELA of *c.* 580, 520 and 480 m for 'MIS 2 stages 3, 4 and 5' respectively, close to our Lg1 and Lg2 ΔELA^{pr} – as close as were their ΔELAs for the MIS 2 maximum.

Table 5. Reconstructed ELAs, and MIS 2 ELA depression with respect to the LIA and present values (ΔELA^{LIA} and ΔELA^{Pr}), in the Altai mountains (m asl).

	ELA					
	MIS 2	LIA	Present	ΔELA^{LIA}	ΔELA^{Pr}	Remarks
Kalguty	2747[1]	3235[1]	3374[3]	488	627	Present: 2010 (Glaciers 1–10)[3]
Tavan Bogd north side	3020[4]	3340[3]	3390[3]	320	370	Present: 2010 (Glaciers 11–26)[3]
Tsagaan Gol-Potanin	2680[5]	3470[5]	3500[3]	790	820	Present: 2010; 3493 in 2008[6]; 3450 in 2011[7]; 3500 (mean for 1980–2018)[8]
Kanas Basin	*c.* 2850[4]		3300[4]		*c.* 450	
South Chuya range	*c.* 2900[4]		*c.*3300[4]		*c.* 400	
Salyugem range	*c.* 2910[4]	3330[2]	3410[2]	*c.* 420	*c.* 500	Present: 2007
Ikh Turgen	2970[4]	3360[2]	3425[2]	390	455	Present: 2011
Mongun-Taiga	2730[9]	3270[9]	3390[9]	540	660	Present: 2013[2]

[1] This study;
[2] Ganyushkin et al. (2015);
[3] Ganyushkin et al. (2018b);
[4] Lehmkuhl et al. (2011);
[5] Radue (2018);
[6] Konya et al. (2013) from Potanin Glacier mass balance;
[7] AAR 0.67 from RGI 6.0;
[8] Khalzan et al. (2022);
[9] Ganyushkin et al. (2018a).

The ELA rise during the Lateglacial was much lower in the Altai Mountains than in the European Alps: +67 m and +174 m for Lg1 and Lg2 after the Kalguty Stage (Table 4), whereas it was in the range +700 to +1200 m in the Alps between the Gschnitz stage (*c.* 17 ka; $\Delta ELA^{LIA} = 600–700$ m), Daun stage (*c.* 14 ka; $\Delta ELA^{LIA} = 400–500$ m) and the Egesen maximum (*c.* 12.5 ka; $\Delta ELA^{LIA} = 250–350$ m; Ivy-Ochs, 2015) – Kalguty Lg1 and Lg2 could correspond to these Alpine Daun and Egesen stages.

Conclusions

The advances of the valley glacier that built a wide terminal morainic complex and lateral kame terraces in the upper Kalguty basin and flowed toward the south-east through the Ulan-Dawa pass correspond to an MIS 2 maximum stage (Kalguty Stage) that occurred prior to 21 ka and probably prior to 22.5 ka; its ELA depression compared to the LIA ELA was *c.* 530 m. A rapid retreat of the low-gradient Kalguty Glacier occurred after this maximal advance.

A more extended glacier prior to the Kalguty Stage is suggested by (i) till, short moraines and small kame terraces present on the north side of the main valley well above the extent of the Kalguty Stage, and (ii) the wide Kalguty valley downstream from the West morainic complex, where large Pleistocene outlet glaciers flowing from the north side of the Tavan Bogd Ice Cap possibly met the Kalguty Glacier.

After deglaciation of the main valley in the Kalguty basin, individual glaciers stood in the six tributary valleys, the two largest flowing into the Klyuch and Argamji valleys. Two Lateglacial stages (Lg1 and Lg2) have been reconstructed, with a mean ELA depression compared to the LIA ELA of *c.* 420 and 315 m, respectively. They remain undated but could have taken place in the period *c.* 14–12 ka by analogy with stages in the Mongun-Taiga massif, or *c.* 17.5–16 ka as for the Khoton Glacier Lateglacial advances. During the LIA, glaciers retreated in the cirques at the head of the steep valleys of the Saylyugem Range (Fig. S2). The absence of moraine between Lg2 and the LIA suggests that the LIA was the main glacier stage during the Holocene.

The glacier surface area in the upper Kalguty basin decreased from 157 km^2 at the MIS 2 maximum to 5.41 km^2 during the LIA, and to 1.04 km^2 in 2010. Mean elevation change rate for the RGI North Asia region, which includes the Altai Mountains, increased from -0.51 ± 0.2 to -0.70 ± 0.2 m a^{-1} from 2001–2004 to 2015–2019, with higher rates than globally (–0.38 and –0.51 m a^{-1}, respectively; Hugonnet et al., 2021). The few remaining glaciers in the upper Kalguty basin will vanish before 2100, as in most of the Altai Mountains: 93% of the volume of the glaciers located inside the Golden Mountains World Heritage site within the Altai (Russia) are modelled to melt by 2100 according to IPCC RCP8.5 (Bosson et al., 2019).

Our glacier reconstruction further provides a geomorphological and geochronological background to put into context archaeological findings: in this area, the rock art site of Kalgutinskii Rudnik is considered as having Palaeolithic figures, on the basis of stylistic (Molodin & Cheremisin, 1999) and technological features (Cretin et al., 2018). Our results suggest that rock surfaces were accessible for engraving since the end of the LGM.

Acknowledgements. Fieldwork in Altai was funded by the laboratoire international associé Multidisciplinary Research on Prehistoric Art in Eurasia (*Multidisciplinary Research on Prehistoric Art in Eurasia*), and SED dating by a 2016 Université Savoie Mont Blanc grant (ARTMONT). Theia/GEOSUD supplied the SPOT 6/7 and Pléiades Images used for geomorphological mapping. The ASTER AMS national facility (CEREGE, Aix-en-Provence) is supported by the INSU/CNRS, the ANR through the '*Projets thématiques d'excellence*' programme for the '*Equipements d'excellence*' ASTER-CEREGE action and IRD. Dmitry Ganyushkin is acknowledged for a SPOT 5 image from 2010 and the shapefiles of LIA glacier extent, and Natacha Gribenski for helpful discussion on SED data and Altai glacial history. Jürgen Herget, Ross Whitmore and an anonymous reviewer are acknowledged for helping to improve the manuscript by their relevant suggestions. The authors warmly thank Martin Kirkbride for reviewed the English text. This article is dedicated to Didier L. Bourlès, who passed away on 1 March 2021.

Data availability statement

The data that support the findings of this study are available from the corresponding author upon reasonable request.

Conflict of interest—The authors declare that they have no known competing financial interests or personal relationships that could have appeared to influence the work reported in this paper.

Supporting information

Additional supporting information can be found in the online version of this article.

Table S1. Glacier surface area (km^2) for six glacial standstills in the upper Kalguty. MIS 2 maximum (Kalguty Stage) and Lateglacial (Lg1 and Lg2) from *GlaRe* toolbox (except *), LIA and 2010 from Ganyushkin et al. (2018b), and 2016 from RGI 6.0 (RGI Consortium, 2017).

Figure S1. Location of the glaciers in the upper Kalguty basin according to published inventories. LIA (Little Ice Age): Ganyushkin et al. (2018b); 1980: Redkin (1998); 2010: Ganyushkin et al. (2018b); 2016: RGI 6.0 (RGI Consortium, 2017). Background: SPOT5 image from 2010 (contour line interval: 50 m). [1980 inventory: contradictions between map and data table, and inconsistencies with recent inventories and reconstruction of LIA extent, make this inventory unreliable to compare with others.]

Figure S2. Reconstruction of the glacier stillstands during the late Pleistocene in the upper Kalguty. Turquoise: Kalguty Stage (MIS 2 maximum); cyan: Lateglacial 1; blue: Lateglacial 2; pink: LIA; brown: 2010; red: 2016. Orange, red and pink lines: ELA for Kalguty stage, Lg1 and Lg2, respectively. EA: East Argamji; C: Central; T-U: Tundu-Uqgar. MIS 2 maximum, Lg1 and Lg2 from *GlaRe* toolbox; LIA and 2010 from Ganyushkin et al. (2018b); 2016 from RGI 6.0 (RGI Consortium, 2017). Geometry of glacier reconstructions from *GlaRe* was adjusted to the topography of cirques and crests in the valley heads. Contour line interval: 50 m. Map background: shaded 30-m DEM from Aster.

Figure S3. The large valley extending downstream from the reconstructed Kalguty Stage (turquoise) has probably been carved by earlier Pleistocene glaciations. Glaciers on the north side of the Tavan Bogd Massif are much more well developed during the LIA (light blue; Ganyushkin et al., 2018b) and in 2016 (dark blue; RGI 6.0) than the upper Kalguty glaciers; carving deep U-shaped valleys, they were probably the main contributors to glaciations prior to and during MIS 2. Contour line interval: 50 m. Map background: shaded 30-m DEM from Aster.

Abbreviations. LIA, Little Ice Age; MIS, Marine Isotope Stage; LGM, Last Glacial Maximum; ELA, equilibrium line altitude; SED, surface exposure dating; AAR, accumulation area ratio; AABR, accumulation ablation balance ratio; GLOF, glacial lake outburst flood.

References

Agatova, A.R., Nazarov, A.N., Nepop, R.K. & Rodnight, H. (2012) Holocene glacier fluctuations and climate changes in the south-eastern part of the Russian Altai (South Siberia) based on a radiocarbon chronology. *Quaternary Science Reviews*, 43, 74–93. Available at: https://doi.org/10.1016/j.quascirev.2012.04.012

Agatova, A.R., Nepop, R.K., Carling, P.A., Bohorquez, P., Khazin, L.B., Zhdanova, A.N. et al. (2020) Last ice-dammed lake in the Kuray basin, Russian Altai: New results from multidisciplinary research. *Earth-Science Reviews*, 205, 103183. Available at: https://doi.org/10.1016/j.earscirev.2020.103183

Arnold, M., Merchel, S., Bourlès, D.L., Braucher, R., Benedetti, L., Finkel, R.C. et al. (2010) The French accelerator mass spectrometry facility ASTER: Improved performance and developments. *Nuclear Instruments and Methods in Physics Research Section B: Beam Interactions with Materials and Atoms*, 268, 1954–1959. Available at: https://doi.org/10.1016/j.nimb.2010.02.107

Baker, V.R., Benito, G. & Rudoy, A.N. (1993) Paleohydrology of late Pleistocene superflooding, Altay Mountains, Siberia. *Science*, 259, 348–350.

Balco, G., Stone, J.O., Lifton, N.A. & Dunai, T.J. (2008) A complete and easily accessible means of calculating surface exposure ages or erosion rates from ^{10}Be and ^{26}Al measurements. *Quaternary Geochronology*, 3(3), 174–195. Available at: https://doi.org/10.1016/j.quageo.2007.12.001

Batbaatar, J., Gillespie, A.R., Fink, D., Matmon, A. & Fujioka, T. (2018) Asynchronous glaciations in arid continental climate. *Quaternary Science Reviews*, 182, 1–19. Available at: https://doi.org/10.1016/j.quascirev.2017.12.001

Benn, D.I. & Owen, L.A. (1998) The role of the Indian summer monsoon and the mid-latitude westerlies in Himalayan glaciation: review and speculative discussion. *Journal of the Geological Society*, 155, 353–363.

Blomdin, R., Heyman, J., Stroeven, A.P., Hättestrand, C., Harbor, J.M., Gribenski, N. et al. (2016) Glacial geomorphology of the Altai and Western Sayan Mountains, Central Asia. *Journal of Maps*, 12(1), 123–136. Available at: https://doi.org/10.1080/17445647.2014.992177

Blomdin, R., Stroeven, A.P., Harbor, J.M., Gribenski, N., Caffee, M.W., Heyman, J. et al. (2018) Timing and dynamics of glaciation in the Ikh Turgen Mountains, Altai region, high Asia. *Quaternary Geochronology*, 47, 54–71. Available at: https://doi.org/10.1016/j.quageo.2018.05.008

Borchers, B., Marrero, S., Balco, G., Caffee, M., Goehring, B., Lifton, N. et al. (2016) Geological calibration of spallation production rates in the CRONUS-Earth project. *Quaternary Geochronology*, 31, 188–198. Available at: https://doi.org/10.1016/j.quageo.2015.01.009

Bosson, J.-B., Huss, M. & Osipova, E. (2019) Disappearing World Heritage glaciers as a keystone of nature conservation in a changing climate. *Earth's Future*, 7, 469–479. Available at: https://doi.org/10.1029/2018EF001139

Braucher, R., Guillou, V., Bourlès, D.L., Arnold, M., Aumaître, G., Keddadouche, K. et al. (2015) Preparation of ASTER in-house^{10}Be/^{9}Be standard solutions. *Nuclear Instruments and Methods in Physics Research Section B: Beam Interactions with Materials and Atoms*, 361, 335–340. Available at: https://doi.org/10.1016/j.nimb.2015.06.012

Brown, E.T., Edmond, J.M., Raisbeck, G.M., Yiou, F., Kurz, M.D. & Brook, E.J. (1991) Examination of surface exposure ages of Antarctic moraines using in situ produced ^{10}Be and ^{26}Al. *Geochimica et Cosmochimica Acta*, 55, 2269–2283. Available at: https://doi.org/10.1016/0016-7037(91)90103-C

Carling, P., Knaapen, M., Borodavko, P., Herget, J., Koptev, I., Hugenberger, P. et al. (2011) Palaeoshorelines of glacial Lake Kuray–Chuja, south-central Siberia: form, sediments and process. In: Martini, I.P., French, H.M., Perez Alberti, A., (Eds.) *Ice-Marginal and Periglacial Processes and Sediments. Geological Society*, 354. London: Special Publications. pp. 111–128. https://doi.org/10.1144/SP354.1

Chang, J., Wang, N., Li, Z. & Yang, D. (2022) Accelerated Shrinkage of Glaciers in the Altai Mountains from 2000 to 2020, *Front. Earth Sci*, 10, p. 919051. https://doi.org/10.3389/feart.2022.919051

Chen, M., Sun, M., Cai, K., Buslov, M.M., Zhao, G. & Rubanova, E.S. (2014) Geochemical study of the Cambrian–Ordovician meta-sedimentary rocks from the northern Altai-Mongolian terrane, northwestern Central Asian Orogenic Belt: Implications on the provenance and tectonic setting. *Journal of Asian Earth Sciences*, 96, 69–83.

Cheremisin, D.V., Zotkina, L.V., Plisson, H., Cretin, C., Geneste, J.-M., Delannoy, J.-J. et al. (2015) Study of petroglyphs at the Russian Altai in 2015. Problems of Archaeology, Ethnography, Anthropology of Siberia and Neighbouring Territories, 21: 441–445 (in Russian).

Chmeleff, J., von Blanckenburg, F., Kossert, K. & Jakob, D. (2010) Determination of the 10Be half-life by multicollector ICP-MS and liquid scintillation counting. *Nuclear Instruments and Methods in Physics Research Section B: Beam Interactions with Materials and Atoms*, 268, 192–199. Available at https://doi.org/10.1016/j.nimb.2009.09.012

Clark, P.U., Dyke, A.S., Shakun, J.D., Carlson, A.E., Clark, J., Wohlfarth, B. et al. (2009) The last glacial maximum. *Science (New York, N.Y.)*, 325, 710–714. Available at: https://doi.org/10.1126/science.1172873

Corbett, L.B., Bierman, P.R. & Rood, D.H. (2016a) An approach for optimizing in situ cosmogenic ^{10}Be sample preparation. *Quaternary Geochronology*, 33, 24–34. Available at: https://doi.org/10.1016/j.quageo.2016.02.001

Corbett, L.B., Bierman, P.R. & Rood, D.H. (2016b) Constraining multi-stage exposure-burial scenarios for boulders preserved beneath cold-based glacial ice in Thule, northwest Greenland. *Earth and Planetary Science Letters*, 440, 147–157. Available at: https://doi.org/10.1016/j.epsl.2016.02.004

Cretin, C., Geneste, J.-M., Plisson, H., Zotkina, V., Cheremisin, D.V., Molodin, V.I. et al. (2018) Un art rupestre paléolithique au-delà de l'Oural? *Nouvelles de l'archéologie*, 154, 1–13.

Deline, P., Ravanel, L., Delannoy, J.-J., Le Roy, M., Molodin, V.I., Cheremisim, D.V. et al. (2020) Geomorphology of the upper Kalguty Basin, Ukok Plateau, Russian Altai mountains. *Journal of Maps*, 16, 595–604. Available at: https://doi.org/10.1080/17445647.2020.1800529

Delmas, M., Calvet, M., Gunnell, Y., Braucher, R. & Bourlès, D. (2011) Palaeogeography and 10Be exposure-age chronology of Middle and Late Pleistocene glacier systems in the northern Pyrenees: implications for reconstructing regional palaeoclimates. *Palaeogeography, Palaeoclimatology, Palaeoecology*, 305, 109–122. Available at: https://doi.org/10.1016/j.quascirev.2021.106923

Dong, G., Zhou, W., Fu, Y., Zhang, L., Zhao, G. & Li, M. (2020) The last glaciation in the headwater area of the Xiaokelanhe River, Chinese Altai: Evidence from ^{10}Be exposure-ages. *Quaternary Geochronology*, 56, 101054. Available at: https://doi.org/10.1016/j.quageo.2020.101054

Dunne, J., Elmore, D. & Muzikar, P. (1999) Scaling factors for the rates of production of cosmogenic nuclides for geometric shielding and attenuation at depth on sloped surfaces. *Geomorphology*, 27, 3–11.

Earl, L. & Gardner, A. (2016) A satellite-derived glacier inventory for North Asia. *Annals of Glaciology*, 57, 50–60. Available at: https://doi.org/10.3189/2016AoG71A008

Fabel, D., Stroeven, A.P., Harbor, J., Kleman, J., Elmore, D. & Fink, D. (2002) Landscape preservation under Fennoscandian ice sheets determined from in situ produced 10Be and 26Al. *Earth and Planetary Science Letters*, 201, 397–406.

Federici, P.R., Ribolini, A. & Spagnolo, M. (2017) Glacial history of the Maritime Alps from the Last Glacial Maximum to the Little Ice Age. In: Hughes, P.D. & Woodward, J.C., (eds) *Quaternary Glaciation in the Mediterranean Mountains. Geological Society, London, Special Publications*, 433, pp. 137–159. https://doi.org/10.1144/sp433.9

Fenton, C.R., Binnie, S.A., Dunai, T. & Niedermann, S. (2022) The SPICE project: Calibrated cosmogenic 26Al production rates and cross-calibrated 26Al/10Be, 26Al/14C, and 26Al/21Ne ratios in quartz from the SP basalt flow, AZ, USA. *Quaternary Geochronology*, 67, 101218. Available at: https://doi.org/10.1016/j.quageo.2021.101218

Ganiushkin, D., Chistyakov, K. & Kunaeva, E. (2015) Fluctuation of glaciers in the southeast Russian Altai and northwest Mongolia Mountains since the Little Ice Age maximum. *Environmental Earth Sciences*, 74, 1883–1904.

Ganyushkin, D., Chistyakov, K., Volkov, I., Bantcev, D., Kunaeva, E. & Terekhov, A. (2017) Present Glaciers and Their Dynamics in the Arid Parts of the Altai Mountains. *Geosciences*, 7, 117. Available at: https://doi.org/10.3390/geosciences7040117

Ganyushkin, D., Chistyakov, K., Volkov, I., Bantcev, D., Kunaeva, E., Brandová, D. et al. (2018a) Palaeoclimate, glacier and treeline

reconstruction based on geomorphic evidences in the Mongun-Taiga massif (south-eastern Russian Altai) during the Late Pleistocene and Holocene. *Quaternary International*, 470, 26–37.

Ganyushkin, D., Chistyakov, K., Volkov, I., Bantcev, D., Kunaeva, E., Andreeva, T. et al. (2018b) Present Glaciers of Tavan Bogd Massif in the Altai Mountains, Central Asia, and their Changes since the Little Ice Age. *Geosciences*, 8, 414. Available at: https://doi.org/10.3390/geosciences8110414

Ganyushkin, D., Chistyakov, K., Derkach, E., Bantcev, D., Kunaeva, E., Terekhov, A. et al. (2022) Glacier Recession in the Altai Mountains after the LIA Maximum. *Remote Sensing*, 14, 1508. Available at: https://doi.org/10.3390/rs14061508

Gjermundsen, E.F., Briner, J.P., Akçar, N., Foros, J., Kubik, P.W., Salvigsen, O. et al. (2015) Minimal erosion of Arctic alpine topography during late Quaternary glaciation. *Nature Geoscience*, 8, 789–792.

Glorie, S., De Grave, J., Buslov, M.M., Zhimulev, F.I., Izmer, A., Vandoorne, W. et al. (2011) Formation and Palaeozoic evolution of the Gorny-Altai–Altai-Mongolia suture zone (South Siberia): zircon U/Pb constraints on the igneous record. *Gondwana Research*, 20, 465–484.

Gribenski, N., Jansson, K.N., Lukas, S., Stroeven, A.P., Harbor, J.M., Blomdin, R. et al. (2016) Complex patterns of glacier advances during the late glacial in the Chagan Uzun Valley, Russian Altai. *Quaternary Science Reviews*, 149, 288–305. Available at: https://doi.org/10.1016/j.quascirev.2016.07.032

Gribenski, N., Lukas, S., Stroeven, A.P., Jansson, K.N., Harbor, J.M., Blomdin, R. et al. (2017) Reply to comment received from J. Herget et al. regarding "Complex patterns of glacier advances during the late glacial in the Chagan Uzun Valley, Russian Altai. *Quaternary Science Reviews*, 168, 219–221. Available at: https://doi.org/10.1016/j.quascirev.2017.04.013

Gribenski, N., Jansson, K.N., Preusser, F., Harbor, J.M., Stroeven, A.P., Trauerstein, M. et al. (2018) Re-evaluation of MIS 3 glaciation using cosmogenic radionuclide and single grain luminescence ages, Kanas Valley, Chinese Altai. *Journal of Quaternary Science*, 33, 55–67. Available at: https://doi.org/10.1002/jqs.2998

Gruber, S. (2012) Derivation and analysis of a high-resolution estimate of global permafrost zonation. *The Cryosphere*, 6, 221–233. Available at: https://doi.org/10.5194/tc-6-221-2012

GTN-P, (2019) Global Terrestrial Network for Permafrost database: https://gtnp.arcticportal.org/resources/maps/12-resources/37-maps-boreholes. [Accessed 12th January 2019]. 2019

Herget, J., (2005) Reconstruction of Pleistocene ice-dammed lake outburst floods in the Altai Mountains, Siberia. In: Geological Society of America Special Papers, 386: 118 p. https://doi.org/10.1130/0-8137-2386-8.1

Herget, J., Carling, P., Agatova, A., Batbaatar, J., Borodavko, P., Gillespie, A. et al. (2017) Comment on Gribenski, N. et al., 2016. Complex patterns of glacier advances during the late glacial in the Chagan Uzun Valley, Russian Altai. *Quaternary Science Reviews*, 168, 216–219. Available at: https://doi.org/10.1016/j.quascirev.2017.04.014

Herget, J., Agatova, A.R., Carling, P.A. & Nepop, R.K. (2020) Altai megafloods – the temporal context. *Earth-Science Reviews*, 200, 102995. Available at: https://doi.org/10.1016/j.earscirev.2019.102995

Heyman, J., Stroeven, A.P., Harbor, J.M. & Caffee, M.W. (2011) Too young or too old: evaluating cosmogenic exposure dating based on an analysis of compiled boulder exposure ages. *Earth and Planetary Science Letters*, 302, 71–80. Available at: https://doi.org/10.1016/j.epsl.2010.11.040

Heyman, J., Applegate, P.J., Blomdin, R., Gribenski, N., Harbor, J.M. & Stroeven, A.P. (2016) Boulder height – exposure age relationships from a global glacial ^{10}Be compilation. *Quaternary Geochronology*, 34, 1–11. Available at: https://doi.org/10.1016/j.quageo.2016.03.002

Hughes, P.D., Gibbard, P.L. & Ehlers, J. (2013) Timing of glaciation during the last glacial cycle: evaluating the concept of a global 'Last Glacial Maximum' (LGM). *Earth-Science Reviews*, 125, 171–198. Available at: https://doi.org/10.1016/j.earscirev.2013.07.003

Hugonnet, R., McNabb, R., Berthier, E., Menounos, B., Nuth, C., Girod, L. et al. (2021) Accelerated global glacier mass loss in the early twenty-first century. *Nature*, 592, 726–731. Available at: https://doi.org/10.1038/s41586-021-03436-z

Ivy-Ochs, S. (2015) Glacier variations in the European Alps at the end of the last glaciation. *Cuadernos de Investigación Geográfica*, 41, 295–315. Available at: https://doi.org/10.18172/cig.2750

Ivy-Ochs, S., Lucchesi, S., Baggio, P., Fioraso, G., Gianotti, F., Monegato, G. et al. (2018) New geomorphological and chronological constraints for glacial deposits in the Rivoli-Avigliana end-moraine system and the lower Susa Valley (Western Alps, NW Italy): NEW LGM GEOMORPHOLOGY AND CHRONOLOGY IN THE WESTERN ALPS. *Journal of Quaternary Science*, 33, 550–562. Available at: https://doi.org/10.1002/jqs.3034

James, W.H.M., Carrivick, J.L., Quincey, D.J. & Glasser, N.F. (2019) A geomorphology based reconstruction of ice volume distribution at the Last Glacial Maximum across the Southern Alps of New Zealand. *Quaternary Science Reviews*, 219, 20–35. Available at: https://doi.org/10.1016/j.quascirev.2019.06.035

Jones, R.S., Small, D., Cahill, N., Bentley, M.J. & Whitehouse, P.L. (2019) iceTEA: Tools for plotting and analysing cosmogenic-nuclide surface-exposure data from former ice margins. *Quaternary Geochronology*, 51, 72–86. Available at: https://doi.org/10.1016/j.quageo.2019.01.001

Khalzan, P., Sakai, A. & Fujita, K. (2022) Mass Balance of Four Mongolian Glaciers: In-situ Measurements, Long-Term Reconstruction and Sensitivity Analysis. *Frontiers in Earth Science*, 9, 785306. Available at: https://doi.org/10.3389/feart.2021.785306

Khandsuren, P., Seong, Y.B., Oh, J.S., Rhee, H.H., Sandag, K. & Yu, B.Y. (2019) Late Quaternary glacial history of Khentey Mountains, Central Mongolia. *Boreas*, 48, 779–799. Available at: https://doi.org/10.1111/bor.12386

Klinge, M. & Sauer, D. (2019) Spatial pattern of Late Glacial and Holocene climatic and environmental development in Western Mongolia—a critical review and synthesis. *Quaternary Science Reviews*, 210, 26–50. Available at: https://doi.org/10.1016/j.quascirev.2019.02.020

Knudsen, M.F. & Egholm, D.L. (2018) Constraining Quaternary ice covers and erosion rates using cosmogenic 26Al/10Be nuclide concentrations. *Quaternary Science Reviews*, 181, 65–75. Available at: https://doi.org/10.1016/j.quascirev.2017.12.012

Konya, K., Kadota, T., Nakazawa, F., DAVAA, G., PUREVDAGVA, K., Yabuki, H. et al. (2013) Surface mass balance of the Potanin Glacier in the Mongolian Altai Mountains and comparison with Russian Altai glaciers in 2005, 2008, and 2009. *Bulletin of Glaciological Research*, 31, 9–18.

Korschinek, G., Bergmaier, A., Faestermann, T., Gerstmann, U.C., Knie, K., Rugel, G. et al. (2010) A new value for the half-life of ^{10}Be by heavy ion elastic recoil detection and liquid scintillation counting. *Nuclear Instruments and Methods in Physics Research Section B: Beam Interactions with Materials and Atoms*, 268, 187–191. Available at: https://doi.org/10.1016/j.nimb.2009.09.020

Kotljakov, V.M., Kravzova, V.I. & Dreyer, N.N. (1997) *World Atlas of snow and ice resources*. Moscow: Russian Academy of Sciences. p. 392 (In Russian).

Kuhlemann, J., Rohling, E.J., Krumrei, I., Kubik, P., Ivy-Ochs, S. & Kucera, M. (2008) Regional synthesis of Mediterranean atmospheric circulation during the Last Glacial Maximum. *Science*, 321, 1338–1340. Available at: https://doi.org/10.1126/science.1157638

Lal, D. (1991) Cosmic ray labeling of erosion surfaces: in situ nuclide production rates and erosion models. *Earth and Planetary Science Letters*, 104, 424–439. Available at: https://doi.org/10.1016/0012-821X(91)90220-C

Lambeck, K., Rouby, H., Purcell, A., Sun, Y. & Sambridge, M., (2014) Sea level and global ice volumes from the Last Glacial Maximum to the Holocene. *Proceedings of the National Academy of Sciences USA*, 111, 15296–15303. https://doi.org/10.1073/pnas.1411762111.

Lehmkuhl, F. (2008) The kind and distribution of midlatitude periglacial features and Alpine permafrost in Eurasia. In: Kane, D.L., Hinkel, K.M., (Eds.), *Proceedings of the Ninth International Conference on Permafrost*, Fairbanks: 1031–1036.

Lehmkuhl, F., Klinge, M. & Stauch, G. (2004) The extent of Late Pleistocene glaciations in the Altai and Khangai Mountains. In: Ehlers, J. & Gibbard, P.L., (Eds.) *Quaternary Glaciations: Extent and*

Chronologies, Part III: South America, Asia, Africa, Australia, Antarctica. Amsterdam: Elsevier. pp. 243–254.

Lehmkuhl, F., Klinge, M. & Stauch, G. (2011) The extent and timing of Late Pleistocene Glaciations in the Altai and neighboring mountains systems. In: Ehlers, J. & Gibbards, P.L., (Eds.) *Quaternary Glaciations: Extent and Chronology - A Closer Look*, 15. Amsterdam: Elsevier. pp. 967–979.

Lehmkuhl, F., Klinge, M., Rother, H. & Hülle, D. (2016) Distribution and timing of Holocene and late Pleistocene glacier fluctuations in western Mongolia. *Annals of Glaciology*, 57(71), 169–178. Available at: https://doi.org/10.3189/2016AoG71A030

Lifton, N., Sato, T. & Dunai, T.J. (2014) Scaling in situ cosmogenic nuclide production rates using analytical approximations to atmospheric cosmic-ray fluxes. *Earth and Planetary Science Letters*, 386, 149–160. Available at: https://doi.org/10.1016/j.epsl.2013.10.052

Mackintosh, A.N., Anderson, B.M. & Pierrehumbert, R.T. (2017) Reconstructing Climate from Glaciers. *Annual Review of Earth and Planetary Sciences*, 45, 649–680. Available at: https://doi.org/10.1146/annurev-earth-063016-020643

Marchenko, S., Ishikawa, M., Sharkhuu, N., Jin, H., Li, X., Lin, Z. et al. (2006) Distribution and Monitoring of Permafrost in Central and Eastern Asia. Workshop on Permafrost of Central and Eastern Asia Report, Lanzhou: p 4.

Marrero, S.M., Phillips, F.M., Borchers, B., Lifton, N., Aumer, R. & Balco, G. (2016) Cosmogenic nuclide systematics and the CRONUScalc program. *Quaternary Geochronology*, 31, 160–187. Available at: https://doi.org/10.1016/j.quageo.2015.09.0

Martinson, D.G., Pisias, N.G., Hays, J.D., Imbrie, J., Moore, T.C. & Shackleton, N.J. (1987) Age Dating and the Orbital Theory of the Ice Ages: Development of a High-Resolution 0 to 300,000-Year Chronostratigraphy. *Quaternary Research*, 27, 1–29. Available at: https://doi.org/10.1016/0033-5894(87)90046-9

Merchel, S. & Herpers, U. (1999) An update on radiochemical separation techniques for the determination of long-lived radionuclides via accelerator mass spectrometry. *ract*, 84, 215–220.

Merchel, S. & Bremser, W. (2004) First international ^{26}Al interlaboratory comparison – Part I. *Nuclear Instruments and Methods in Physics Research Section B: Beam Interactions with Materials and Atoms*, 223-224, 393–400. Available at: https://doi.org/10.1016/j.nimb.2004.04.076

Merchel, S., Arnold, M., Aumaître, G., Benedetti, L., Bourlès, D.L., Braucher, R. et al. (2008) Towards more precise 10Be and 36Cl data from measurements at the 10-14 level: influence of sample preparation. *Nuclear Instruments and Methods in Physics Research Section B: Beam Interactions with Materials and Atoms*, 266(22), 4921–4926. Available at: https://doi.org/10.1016/j.nimb.2008.07.031

Molodin, V.I. & Cheremisin, D.V. (1999) *The most ancient rock drawings of the Ukok plateau*. Novosibirsk: Nauka. p. 160. (in Russian).

Monegato, G. (2012) Local glaciers in the Julian Prealps (NE italy) during the Last Glacial Maximum. *Alpine and Mediterranean Quaternary*, 25(1), 5–14.

Moskalenko, I.G., Ganyushkin, D.A. & Chistyakov, K.V. (2013) Modern and ancient glaciation of northern slope of the Tavan-Bogdo-Ola massif. *Ice and Snow*, 3, 33–44 (in Russian).

Nishiizumi, K., Kohl, C.P., Arnold, J.R., Dorn, R., Klein, I., Fink, D. et al. (1993) Role of in situ cosmogenic nuclides ^{10}Be and ^{26}Al in the study of diverse geomorphic processes. *Earth Surface Processes and Landforms*, 18, 407–425.

Pallàs, R., Rodés, Á., Braucher, R., Bourlès, D., Delmas, M., Calvet, M. et al. (2010) Small, isolated glacial catchments as priority targets for cosmogenic surface exposure dating of Pleistocene climate fluctuations, southeastern Pyrenees. *Geology*, 38(10), 891–894. Available at: https://doi.org/10.1130/G31164.1

Parzinger, H. (2017) Burial mounds of Scythian elites in the Eurasian steppe: New discoveries. *Journal of the British Academy*, 5, 331–355. Available at: https://doi.org/10.85871/jba/005.331

Paterson, W.S.B. (1994) *The physics of glaciers*. Oxford: Elsevier. p. 480. https://doi.org/10.1016/C2009-0-14802-X

Paul, F., Rastner, P., Azzoni, R.S., Diolaiuti, G., Fugazza, D., Le Bris, R. et al. (2020) Glacier shrinkage in the Alps continues unabated as revealed by a new glacier inventory from Sentinel-2. *Earth System Science Data*, 12, 1805–1821. Available at: https://doi.org/10.5194/essd-12-1805-2020

Pellitero, R., Rea, B., Spagnolo, M., Bakke, J., Hughes, P., Ivy-Ochs, S. et al. (2015) A GIS tool for automatic calculation of glacier equilibrium-line altitudes. *Computers & Geosciences*, 82, 55–62. Available at: https://doi.org/10.1016/j.cageo.2015.05.005

Pellitero, R., Rea, B.R., Spagnolo, M., Bakke, J., Ivy-Ochs, S., Frew, C.R. et al. (2016) GlaRe, a GIS tool to reconstruct the 3D surface of palaeoglaciers. *Computers & Geosciences*, 94, 77–85. Available at: https://doi.org/10.1016/j.cageo.2016.06.008

Prud'homme, C., Vassallo, R., Crouzet, C., Carcaillet, J., Mugnier, J.-L. & Cortés-Aranda, J. (2020) Paired10Be sampling of polished bedrock and erratic boulders to improve dating of glacial landforms: an example from the Western Alps. *Earth Surface Processes and Landforms*, 45, 1168–1180. Available at: https://doi.org/10.1002/esp.4790

Radue, M.J., (2018) Glacial History of the Tsagaan Gol-Potanin Glacier Valley, Altai Mountains, Mongolia. MSc thesis, University of Maine. https://digitalcommons.library.umaine.edu/etd/2865

Rea, B.R. (2009) Defining modern day Area-Altitude Balance Ratios (AABRs) and their use in glacier-climate reconstructions. *Quaternary Science Reviews*, 28, 237–248. Available at: https://doi.org/10.1016/j.quascirev.2008.10.011

Redkin, A.G. (1998) Natural conditions of the Ukok Plateau during the Pleistocene and the Holocene. PhD thesis, University of Barnaul, 174 p. (in Russian).

Reuther, A.U., Herget, J., Ivy-Ochs, S., Borodavko, P., Kubik, P.W. & Heine, K. (2006) Constraining the timing of the most recent cataclysmic flood event from icedammed lakes in the Russian Altai Mountains, Siberia, using cosmogenic in situ ^{10}Be. *Geology*, 34, 913–916. Available at: https://doi.org/10.1130/G22755A.1

RGI Consortium, (2017) Randolph Glacier Inventory (RGI) – A Dataset of Global Glacier Outlines: Version 6.0. Technical Report, Global Land Ice Measurements from Space, Boulder. Digital Media. https://doi.org/10.7265/N5-RGI-60

Riseborough, D., Shiklomanov, N., Etzelmüller, B., Gruber, S. & Marchenko, S. (2008) Recent advances in permafrost modelling. *Permafrost and Periglacial Processes*, 19, 137–156. Available at: https://doi.org/10.1002/ppp.615

Rudoy, A.N. (2002) Glacier-dammed lakes and geological work of glacial superfloods in the Late Pleistocene, southern Siberia, Altai Mountains. *Quaternary International*, 87, 119–140.

Ruszkiczay-Rüdiger, Z., Neuhuber, S., Braucher, R., Lachner, J., Steier, P., Wieser, A. et al. (2021) Comparison and performance of two cosmogenic nuclide sample preparation procedures of in situ produced ^{10}Be and ^{26}Al. *Journal of Radioanalytical and Nuclear Chemistry*, 329, 1523–1536. Available at: https://doi.org/10.1007/s10967-021-07916-4

Samworth, E.A., Warburton, E.K. & Engelbertink, G.A.P. (1972) Beta Decay of the Al 26 Ground State. *Physical Review C*, 5, 138–142. Available at: https://doi.org/10.1103/PhysRevC.5.138

Sanchez Goñi, M.F. & Harrison, S.P. (2010) Millennial-scale climate variability and vegetation changes during the Last Glacial: concepts and terminology. *Quaternary Science Reviews*, 29, 2823–2827. Available at: https://doi.org/10.1016/j.quascirev.2009.11.014

Serra, E., Valla, P.G., Gribenski, N., Carcaillet, J. & Deline, P. (2022) Post-LGM glacial and geomorphic evolution of the Dora Baltea valley (western Italian Alps). *Quaternary Science Reviews*, 282, 107446.

Shahgedanova, M., Nosenko, G., Khromova, T. & Muraveyev, A. (2010) Glacier shrinkage and climatic change in the Russian Altai from the mid-20th century: An assessment using remote sensing and PRECIS regional climate model. *Journal of Geophysical Research*, 115, D16107. Available at: https://doi.org/10.1029/2009JD012976

Shilling, D.H. & Hollin, J.T. (1981) Numerical reconstructions of valley glaciers and small ice caps. In: Denton, G.H. & Hughes, T.J., (Eds.) *The Last Great Ice Sheets*. New York: Wiley. pp. 207–220.

Siman-Tov, S., Stock, G.M., Brodsky, E.E. & White, J.C. (2017) The coating layer of glacial polish. *Geology*, 45(11), 987–990. Available at: https://doi.org/10.1130/G39281.1

Slon, V., Mafessoni, F., Vernot, B., de Filippo, C., Grote, S., Viola, B. et al. (2018) The genome of the offspring of a Neanderthal mother

and a Denisovan father. *Nature*, 561, 113–116. Available at: https://doi.org/10.1038/s41586-018-0455-x

Stone, J.O. (2000) Air pressure and cosmogenic isotope production. *Journal of Geophysical Research: Solid Earth*, 105, 23753–759.

Strand, P.D., Putnam, A.E., Sambuu, O., Putnam, D.E., Denton, G.H., Schaefer, J.M. et al. (2022) A ^{10}Be Moraine Chronology of the Last Glaciation and Termination at 49°N in the Mongolian Altai of Central Asia. *Paleoceanography and Paleoclimatology*, 37(5), e2022PA004423 Available at: https://doi.org/10.1029/2022PA004423

Svistunov, M.I., Kurbanov, R.N., Murray, A.S., Taratunina, N.A., Semikolennykh, D.V., Entin, A.L. et al. (2022) Constraining the age of Quaternary megafloods in the Altai Mountains (Russia) using luminescence. *Quaternary Geochronology*, 73, 101399. Available at: https://doi.org/10.1016/j.quageo.2022.101399

Taylor, W., Hart, I., Pan, C., Bayarsaikhan, J., Murdoch, J., Caspari, G. et al. (2021) High altitude hunting, climate change, and pastoral resilience in eastern Eurasia. *Scientific Reports*, 11, 14287. Available at: https://doi.org/10.1038/s41598-021-93765-w

Thompson, L.G., Davis, M.E., Mosley-Thompson, E., Lin, P.N., Henderson, K.A. & Mashiotta, T.A. (2005) Tropical ice core records: evidence for asynchronous glaciation on Milankovitch timescales. *Journal of Quaternary Science*, 20, 723–733. Available at: https://doi.org/10.1002/jqs.972

Walther, M., Dashtseren, A., Kamp, U., Temujin, K., Meixner, F., Pan, C.G. et al. (2017) Glaciers, permafrost and lake levels at the Tsengel Khairkhan Massif, Mongolian Altai, during the Late Pleistocene and Holocene. *Geosciences*, 7, 73. Available at: https://doi.org/10.3390/geosciences7030073

WGMS. (2021) *Fluctuations of Glaciers Database*. Zurich, Switzerland: World Glacier Monitoring Service. Available at: https://doi.org/10.5904/wgms-fog-2021-05

Xu, X., Yang, J., Dong, G., Wang, L. & Miller, L. (2009) OSL dating of glacier extent during the Last Glacial and the Kanas Lake basin formation in Kanas River valley, Altai Mountains, China. *Geomorphology*, 112, 306–317. Available at: https://doi.org/10.1016/j.geomorph.2009.06.016

Zhao, J., Yin, X., Harbor, J.M., Lai, Z., Liu, S. & Li, Z. (2013) Quaternary glacial chronology of the Kanas River valley, Altai Mountains, China. *Quaternary International*, 311, 44–53. Available at: https://doi.org/10.1016/j.quaint.2013.07.047